CrossMark

J. Fluid Mech. (2018), *vol.* 836, *pp.* 873–909. © Cambridge University Press 2017
doi:10.1017/jfm.2017.815

Understanding evolution of vortex rings in viscous fluids

Aashay Tinaikar[1,†], **S. Advaith**[1] **and S. Basu**[1,2]

[1]Interdisciplinary Centre for Energy Research, Indian Institute of Science, Bangalore-560012, Karnataka, India

[2]Department of Mechanical Engineering, Indian Institute of Science, Bangalore-560012, Karnataka, India

(Received 2 June 2017; revised 21 September 2017; accepted 7 November 2017; first published online 13 December 2017)

The evolution of vortex rings in isodensity and isoviscosity fluid has been studied analytically using a novel mathematical model. The model predicts the spatiotemporal variation in peak vorticity, circulation, vortex size and spacing based on instantaneous vortex parameters. This proposed model is quantitatively verified using experimental measurements. Experiments are conducted using high-speed particle image velocimetry (PIV) and laser induced fluorescence (LIF) techniques. Non-buoyant vortex rings are generated from a nozzle using a constant hydrostatic pressure tank. The vortex Reynolds number based on circulation (Γ/ν) is varied in the range 100–1500 to account for a large range of operating conditions. Experimental results show good agreement with theoretical predictions. However, it is observed that neither Saffman's thin-core model nor the thick-core equations could correctly explain vortex evolution for all initial conditions. Therefore, a transitional theory is framed using force balance equations which seamlessly integrate short- and long-time asymptotic theories. It is found that the parameter $A = (a/\sigma)^2$, where a is the vortex half-spacing and σ denotes the standard deviation of the Gaussian vorticity profile, governs the regime of vortex evolution. For higher values of A, evolution follows short-time behaviour, while for $A = O(1)$, long-time behaviour is prominent. Using this theory, many reported anomalous observations have been explained.

Key words: vortex dynamics, vortex flows, vortex streets

1. Introduction

Vortex rings are ubiquitous in classical fluid mechanics. They are central to many natural and artificial fluid dynamic processes (Hill 1975; Dengler & Reeder 1997; Spalart 1998; Emanuel 2005; Smith, Montgomery & Zhu 2005). Vortices are formed due to various mechanisms that span disparate physical domains (Rayfield & Reif 1964; Thomson & Newall 1885; Dahm, Scheil & Tryggvason 1989; Lee *et al.* 2015; Manu *et al.* 2015). In addition to the above, the study of vortex rings has attracted many researchers due to their notable existence, at different spatiotemporal scales, in fluid flow (She, Jackson & Orszag 1990; Pullin & Saffman 1998).

† Email address for correspondence: tinaikar.aashay@gmail.com

https://doi.org/10.1017/jfm.2017.815 Published online by Cambridge University Press

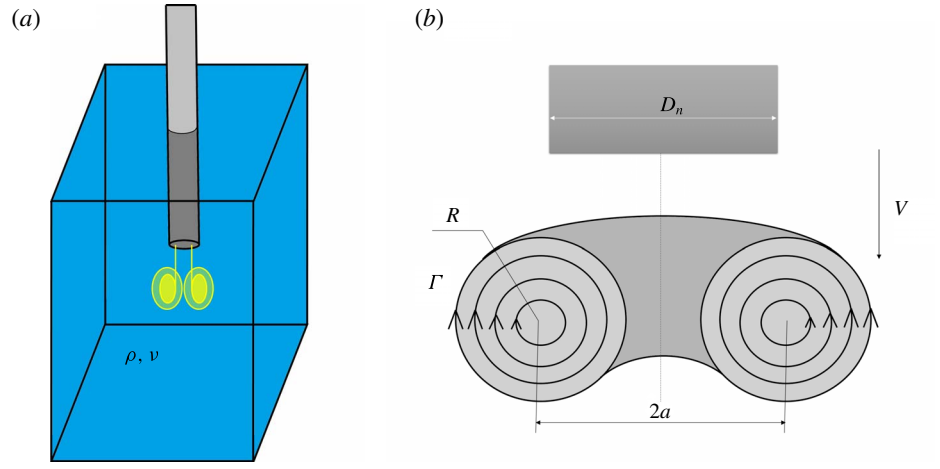


FIGURE 1. (Colour online) Schematic of vortex ring generation and vortex parameters.

Vortex interactions have also been found to play a major role in various fluid dynamic and heat transfer processes. Once formed, vortex rings are self-sustained and self-propelled. Propulsive features are characteristic to vortex shedding and resultant coherent structures (Turner 1960; Fohl 1967; Spedding, Hedenström & Rosén 2003; Dabiri & Gharib 2005). Thus, vortex shedding has been found of significance in a variety of engineering applications (e.g. transportation, flow control) as well as in biological systems (e.g. fish swimming and insect flight) (Moore & Saffman 1973; Weihs 1973; Lugt 1983; Dabiri 2009). A number of studies (Gharib *et al.* 2006; Arvidsson *et al.* 2016) have also highlighted the importance of vortical flows for the diagnosis of various ailments.

Laboratory experiments on vortex rings are usually performed to understand vortex formation, evolution, interaction and decay. Vortices are usually formed by forcing bulk fluid through a constricted opening such as an orifice or a nozzle. Recent studies by Gharib, Rambod & Shariff (1998) showed that there is a maximum cap on the circulation that can be induced by a single vortex ring. According to this study, a single vortex is obtained for values of $L/D_n < 4$, where L is the stroke length and D_n is the internal nozzle diameter. The concept of the formation number (FN; L/D_n) can be effectively extended to other experimental configurations as well.

Analytical studies concerning vortex ring evolution can be traced back to the work of Helmholtz (1858) and Kelvin (1867). Early theoretical studies on the formation and evolution of vortex rings (assuming inviscid behaviour) were conducted by Lamb (1932) and Sommerfeld (1950). Studies show that a fully developed axisymmetric vortex is governed by two parameters, namely the vorticity distribution and the toroidal radius, as shown in figure 1. Dyson (1893) and Fraenkel (1972), through rigorous mathematical formulations, coined expressions for the translational velocity of inviscid thin vortex rings.

Detailed studies of vortex translation in viscous fluid were conducted by Saffman (1970) and Pullin (1979), where they assumed a vorticity distribution as given by Lamb–Oseen (1.1)

$$\omega(r, t) = \frac{\Gamma_0}{4\pi\nu t} \mathrm{e}^{-(r^2/4\nu t)}. \tag{1.1}$$

https://doi.org/10.1017/jfm.2017.815 Published online by Cambridge University Press

Here, Γ_0 stands for initial circulation while ω, ν, r and t represent the vorticity distribution, kinematic viscosity of the fluid, radial distance from the core centre and time, respectively. Using this, Saffman also derived the vortex propagation velocity to the first order, given by

$$V = \frac{\Gamma_0}{4\pi a_0}\left[\ln\left(\frac{8a_0}{\sqrt{4\nu t}}\right) - 0.558 + O\left\{\left(\frac{\nu t}{a_0^2}\right)^{1/2}\ln\left(\frac{\nu t}{a_0^2}\right)\right\}\right], \tag{1.2}$$

where the expression for the Saffman core radius is given by $r_{cs} = \sqrt{4\nu t}$. These equations are valid for finite core sizes in viscous fluids for small time values, typically for $t \ll T$, where T is the piston stroke time. The above results were derived considering (1.1), for which circulation turns out to be

$$\Gamma = \int_0^\infty \omega \, \mathrm{d}\psi = \text{const.}, \tag{1.3}$$

where ψ stands for the area of selected contour. Thus, constant circulation, when coupled with the concept of a constant hydrodynamic impulse, mandates that the vortex ring diameter should remain invariant in time. Thus, the thin-core model proposed by Saffman could not account for the decreasing circulation or ring expansion as observed in the experiments. However, using an order of magnitude argument, Saffman proposed relations for the translational velocity V and radius a for thick rings at longer times:

$$a^2 \approx a_0^2 + k'\nu t \tag{1.4}$$

$$V \approx \frac{I}{k}(a_0^2 + k'\nu t)^{-3/2}. \tag{1.5}$$

Here, I stands for the impulse of the vortex ring and k and (k') are constants. This aspect was further explored by Maxworthy (1972, 1977), where he performed multiple experiments on laminar vortex rings ($Re < 600$). He reported overprediction in the ring expansion as given by (1.4). Using his entrainment model, he tried to explain the changes in vortex parameters and provided relations for vortex size, circulation and convective velocity:

$$a \propto t^{1/3}, \quad \Gamma \propto t^{-2/3}, \quad V \propto t^{-1}. \tag{1.6a–c}$$

Maxworthy arrived at these empirical relations using scaling arguments and dimensional analysis. This subject was later addressed by the work of Cantwell & Rott (1988), Stanaway, Cantwell & Spalart (1988) and Fukumoto & Moffatt (2000) using numerical methods. These findings found corroboration with some of the existing theories. However, their model still lacked universal applicability and could not explain the dynamics for a wide range of Reynolds numbers. These studies thus show the lack of consensus among the proposed theories.

The above-mentioned vortex parameters, though intuitively complex, greatly influence vortex interactions with thermal and density stratifications ubiquitous in nature (Linden 1973; Dahm *et al.* 1989; Orlandi, Egermann & Hopfinger 1998; Advaith *et al.* 2017). Though the significance of these variables has been long known, there have been only a very limited number of studies incorporating their effects. The major reason for this lack of attention is the complex nature of vortex evolution.

https://doi.org/10.1017/jfm.2017.815 Published online by Cambridge University Press

Recently, many analytical and numerical studies pertaining to vortex evolution have succeeded in arriving at a near accurate estimation of the vortex parameters (Bergdorf, Koumoutsakos & Leonard 2007). However, these equations are either mathematically complex or iterative, and hence provide limited physical insights into phenomena such as vortex interactions.

A detailed review of available theories and their results are included in supplementary material available at https://doi.org/10.1017/jfm.2017.815. In summary, most of the analytical studies on vortex evolution have focused on the asymptotic behaviours of its lifetime. At the lower end, studies have been conducted for thin vortex rings using the classical vorticity equation of Lamb–Oseen (1.1). At the other end, almost all the studies resort to conservation of hydrodynamic impulse to arrive at the long-time behaviour. These two extreme approaches are, however, fundamentally different from each other. Rarely there have been efforts to link the two. Moreover, any attempts in this direction have been unfruitful, and thus the transformation of short-time equations into the long-time regime is a problem, still unresolved. In addition, many different forms of viscous time scales have been used throughout the literature. Parameters such as circulation (Γ), viscosity (ν), ring radius (a) and nozzle diameter (D_n) have been used casually and interchangeably, primarily aimed at normalization, with minimal insights. Thus, the available time scales are far from universal and do not successfully explain vortex evolution.

Here we try to comprehend the mechanism of vortex evolution in viscous fluids using a simple mathematical framework. This paper is divided into five sections, with § 1 being the introduction. In § 2, we try to frame simple approximated mathematical equations describing each parameter of the vortex rings. We will also try to give physical insights into vorticity diffusion and ring expansion. Details about the experimental set-up, visualization techniques and test cases will be described in § 3. In § 4, we provide the results of our experimental studies. These datasets will be compared with our theoretical predictions and results already available in the literature. Discussions about the results, including their range of validity, will be conducted in § 5. In § 6, we will summarize our study and discuss its implications.

2. Mathematical formulation

Vortex rings are formed in lab settings by impulsive ejection of fluid through a nozzle opening, as shown in figure 1. The ejected fluid rolls up to form vortex rings (Didden 1979; Auerbach 1988). During the initial period, vortex rings are unstable, with continuous momentum addition and significant viscous effects. We define this period as 'formation time', within which the vortex parameters are governed by initial operating conditions such as stroke length L, transient velocity and nozzle geometry. It should be noted that this definition is not to be confused with the terminology defined by Gharib *et al.* (1998), where he defined formation time (L/D_n) as the maximum stroke time permitted for evolution of a single vortex ring. Some basic observations describing vortex formation are elucidated in § 4.1.

Beyond 'formation time', the vortex ring stabilizes and attains a smooth vorticity distribution. These vortex rings then move with a self-induced velocity. For inviscid fluids, (after neglecting any instabilities) the vortex does not diffuse, resulting in a consistent vorticity distribution throughout its period of propagation. However, for real fluids with finite viscosity, diffusion gives rise to time-variant vorticity fields. This varying vorticity can be best understood by examining the vorticity transport equation given by

$$\frac{\mathrm{D}\omega}{\mathrm{D}t} = (\omega \cdot \nabla)u - \frac{\nabla\rho}{\rho} \times \frac{\mathrm{D}u}{\mathrm{D}t} - g\frac{\nabla\rho}{\rho} \times \boldsymbol{j} + \nu\nabla^2\omega. \tag{2.1}$$

https://doi.org/10.1017/jfm.2017.815 Published online by Cambridge University Press

In the above, $\boldsymbol{j}$ denotes a unit vector in the vertical direction while the other variables carry their usual meaning. The first term on the right denotes the vortex turning and stretching term, while the last term of the equation captures vorticity generation due to diffusion. The second and third terms on the right-hand side characterize the baroclinic generation of vorticity due to hydrostatic and hydrodynamic forces. These baroclinic vorticity terms reduce to zero for the constant-density fluid domain. Similarly, the vortex turning and stretching terms vanish for two-dimensional (2D) flows.

Even though vortex rings are three-dimensional structures, most of the insights into vortex evolution can be obtained by neglecting the curvature effects and treating 2D viscous diffusion as the dominant mechanism (Oseen 1910; Lamb 1932). Thus, a 2D axisymmetric vortex pair descending in a homogeneous incompressible fluid can be defined by (2.2), where the effects of convective velocity on vortex deformation are neglected. The vorticity transport can then be modelled in polar coordinates as a simple diffusion equation:

$$\frac{\partial \omega}{\partial t} = \nu \nabla^2 \omega = \nu \left(\frac{\partial^2 \omega}{\partial r^2} + \frac{1}{r} \frac{\partial \omega}{\partial r} \right). \tag{2.2}$$

The standard procedure for solving the above equation involves the concept of similarity variables, where the implicit variables r and t are interlinked using a new variable η. The solution yields a pure tangential velocity field. Therefore, this explicit Gaussian profile forms the solution of the complete vorticity equation rather than just its linear approximation.

$$\omega(r, t) = \omega_m(t) \mathrm{e}^{-(r/\sigma(t))^2}. \tag{2.3}$$

2.1. *Limitations of the short-time, self-similarity solution*

The solution to vorticity diffusion (2.2) using self-similarity variables results in the Lamb–Oseen equation given by

$$\omega(r, t) = \frac{\Gamma_0}{4\pi \nu t} \mathrm{e}^{-(r^2/4\nu t)} \tag{2.4}$$

This solution is obtained on the premise of the idealized condition of a highly localized initial vorticity distribution given by a Dirac delta function. Thus, the above equation describes the phenomenon under specialized conditions only. However, in reality, vortex rings generated from the nozzle exit rarely possess such concentrated cores. The vorticity is typically diffused over a finite spatial domain. Thus, for practical cases, we are more interested in finding solutions to the diffusion equation with finite-sized vorticity cores. Similar problems have been studied in great detail by Barenblatt (1996). Therefore, for such initially thick vortex cores of size r_c, the solution depends on the additional dimensionless group

$$\pi = \frac{r_c^2}{\nu t}. \tag{2.5}$$

The parameter r_c spoils the self-similarity of the solution, since the solution can no longer be defined by a single dimensionless parameter. Under such conditions,

$$\omega(r, t) = t^{-m} f(\eta, \pi). \tag{2.6}$$

General solutions to such finite-size diffusion problems are not exact similarity ones (Witelski & Bernoff 1998); however, under appropriate assumptions, asymptotic limits yield such special solutions.

https://doi.org/10.1017/jfm.2017.815 Published online by Cambridge University Press

2.2. *Approximate solutions to the vorticity equations*

Consider a fully developed vortex at any particular time instant defined by (2.7). The vorticity and velocity fields for such a vortex are shown in figure 2. Vorticity diffusion in any Newtonian fluid is governed by viscous shear forces given by (2.8)

$$\omega_t(r) = \omega_{m,t} \mathrm{e}^{-(r/\sigma_t)^2} \tag{2.7}$$

$$\tau_t(r) = \mu \left(\frac{\partial V}{\partial r} \right). \tag{2.8}$$

Please note that the angular momentum (Ω) is equal to half of the vorticity. However, this numerical factor is neglected throughout this paper. Thus, for a fluid region defined as a disk of radius r, as in figure 2, viscous stress at any time instant t due to external shear can be calculated as

$$\tau_t(r) = \mu \left(\frac{\partial r\omega}{\partial r} \right) = \mu \left[r\frac{\partial \omega}{\partial r} + \omega \right] \tag{2.9}$$

$$\tau_t(r) = -\mu \left[\omega_{m,t} \mathrm{e}^{-(r/\sigma_t)^2} \left(1 - \frac{2r^2}{\sigma_t^2} \right) \right], \tag{2.10}$$

where μ is the dynamic viscosity. For a stable Gaussian vorticity profile (2.7), the velocity variation is shown in figure 2. It is evident that the maximum fluid velocity occurs at a distance $\sigma/\sqrt{2}$ from the vortex centre. This results in complex shear interactions resulting in vorticity diffusion, internal as well as external to the locus of maximum velocity. Some prior studies regarding the evolution of Gaussian vortex rings have accounted for external as well as internal expansion of the core structure (Fraenkel 1972; Fukumoto & Moffatt 2000). However, numerical and experimental studies clearly show a decreasing trend in peak vorticity values and a corresponding increase in the length scale of the vorticity distribution throughout its propagation period. Previous studies also validate the claim that a fully developed vortex ring is characterized by a vorticity distribution which can be best approximated by a Gaussian profile (Saffman 1978; Weigand & Gharib 1997). Thus, using known parameters, we propose a simpler vortex evolution model by considering only the external expansion of the vortex core. Internal interaction of the core structure is neglected and assumed to adjust itself to satisfy the Gaussian vorticity distribution parameters.

Consider the core to be a rigid disc with an approximately linear ω variation (2.11) and radius ϵ, as shown in figure 3. Let an arbitrary definition of the vortex core size correspond to $\epsilon = k_1\sigma$ and $\omega(\epsilon) = k_2\omega_m$, where $k_2 = \mathrm{e}^{-(k_1)^2}$. The vorticity distribution and angular momentum of this disc are given by

$$\omega_t(r) = \omega_{m,t} \left[1 - \frac{1-k_2}{k_1} \frac{r}{\sigma_t} \right] \tag{2.11}$$

$$L = \int \mathrm{d}I\, \omega_t(r) = \int_0^{\epsilon} \rho(2\pi r\, \mathrm{d}r\, \mathrm{d}z)(r^2)\omega_{m,t} \left[1 - \frac{1-k_2}{k_1} \frac{r}{\sigma_t} \right]. \tag{2.12}$$

This above vortex disc can be defined by an average vorticity given by

$$I\omega_{avg,t} = \left(\frac{\rho\pi\epsilon^4\, \mathrm{d}z}{2} \right) \omega_{avg,t} = L, \tag{2.13}$$

which yields

$$\omega_{avg,t} = \omega_{m,t} \left[1 - \frac{4(1-k_2)}{5} \right]. \tag{2.14}$$

https://doi.org/10.1017/jfm.2017.815 Published online by Cambridge University Press

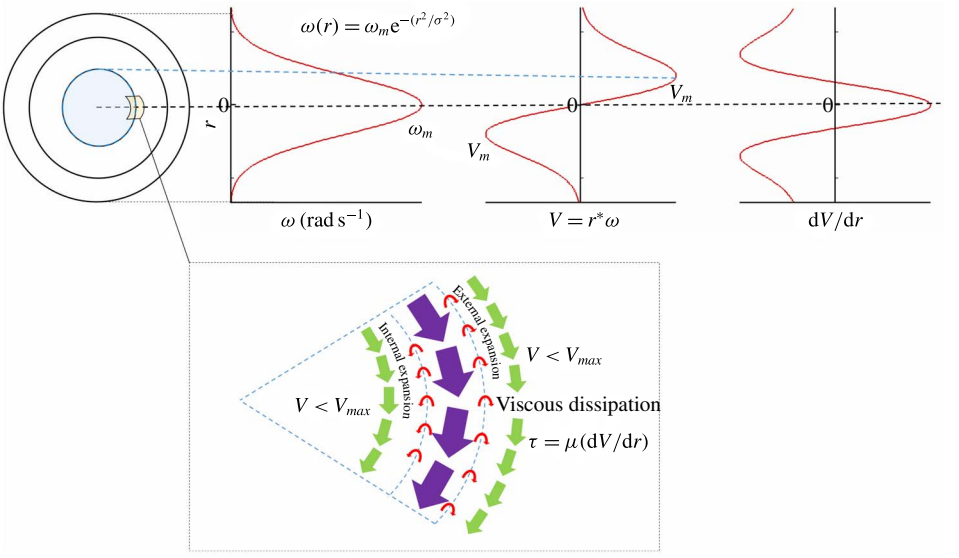


FIGURE 2. (Colour online) Schematic of the vorticity distribution in the core.

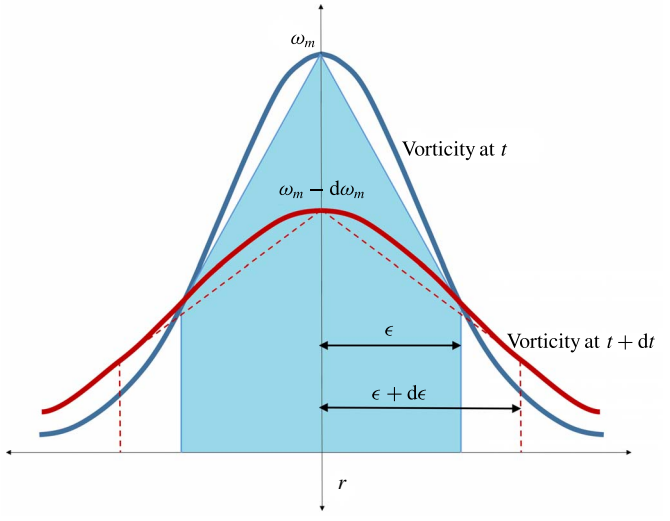


FIGURE 3. (Colour online) Variation of the vorticity distribution with time.

Neglecting any internal fluid interactions, the net torque on the vortex core is given by (2.15). This torque will slow down the vortex core and can be assumed to alter the average vorticity, given by (2.18).

$$T(\epsilon) = -\mu \left| \omega_{m,t} e^{-(\epsilon/\sigma_t)^2} \left(1 - \frac{2\epsilon^2}{\sigma_t^2}\right) \right| (2\pi\epsilon)\epsilon \, dz \tag{2.15}$$

$$\rho \left(\frac{\pi}{2}\epsilon^4 \, dz\right) \alpha_{avg,t} = -\mu \left| \omega_{m,t} e^{-(\epsilon/\sigma_t)^2} \left(1 - \frac{2\epsilon^2}{\sigma_t^2}\right) \right| (2\pi\epsilon)\epsilon \, dz. \tag{2.16}$$

https://doi.org/10.1017/jfm.2017.815 Published online by Cambridge University Press

Substituting the values of $\epsilon = k_1\sigma$ and (2.14), where $k_2 = \mathrm{e}^{-(k_1)^2}$, we get

$$\alpha_{avg,t} = \frac{\partial \omega_{avg,t}}{\partial t} = -4\left|\frac{5(1-2k_1^2)\mathrm{e}^{-k_1^2}}{k_1^2(5-4(1-\mathrm{e}^{-k_1^2}))}\right|\left(\frac{\nu\omega_{avg,t}}{\sigma_t^2}\right), \tag{2.17}$$

which can be written as

$$\frac{\partial \omega_{avg,t}}{\partial t} = -4\phi\left(\frac{\nu\omega_{avg,t}}{\sigma_t^2}\right), \tag{2.18}$$

where

$$\phi = \left|\frac{5(1-2k_1^2)\mathrm{e}^{-k_1^2}}{k_1^2(5-4(1-\mathrm{e}^{-k_1^2}))}\right|. \tag{2.19}$$

Here, the value of ϕ is satisfied by two values of k_1, each on either side of $1/\sqrt{2}$. However, the value of k_1 greater than 0.707 should be accepted. This is because such k_1 values lead to the appropriate sign of velocity gradients pointing away from the vortex core, signifying external dissipation. In contrast, k_1 less than 0.707 signifies internal viscous dissipation, which has been neglected in this derivation.

Thus, at any instant, the rate of decay of peak vorticity is directly proportional to the kinematic viscosity ν and ω_m, and inversely to the variance of the vorticity field. This can be easily understood intuitively. Kinematic viscosity quantifies friction between the fluid layers. Thus, higher friction will lead to greater retardation. Similarly, keeping ν and ω_m constant, concentrated cores will experience greater dissipation due to higher velocity gradients and *vice versa*. At this point, we may be tempted to perform integration to obtain the final expression of peak vorticity $\omega_m(t)$. However, the standard deviation σ is also a time-varying parameter. Hence the expression (2.18) cannot be solved further without understanding the time evolution of σ.

In order to understand the variation in standard deviation σ, we consider the interaction between the core disk and adjacent fluid layer. As a result of the interaction, after time dt, ω_{avg} decreases by dω_{avg} while the core size increases by dϵ. Thus, the new core will have a radius of $(\epsilon + \mathrm{d}\epsilon)$ and a vorticity of $(\omega_{avg} - \mathrm{d}\omega_{avg})$. Using the principle of conservation of angular momentum and neglecting higher-order terms, we get

$$I_{ini}\omega_{ini} = I_{fi}\omega_{fi} \tag{2.20}$$

$$\rho\left(\frac{\pi}{2}\right)\epsilon^4\omega_{avg,t} = \rho\left(\frac{\pi}{2}\right)(\epsilon+\mathrm{d}\epsilon)^4(\omega_{avg,t} - \mathrm{d}\omega_{avg,t}) \tag{2.21}$$

$$k_1^4\epsilon^4\omega_{avg,t} = k_1^4(\sigma_t^4 + 4\sigma_t^2\,\mathrm{d}\sigma_t)\left(\omega_{avg,t} - \omega_{avg,t}4\phi\left(\frac{\nu}{\sigma_t^2}\right)\mathrm{d}t\right) \tag{2.22}$$

$$\frac{\mathrm{d}\sigma_t}{\mathrm{d}t} = \phi\left(\frac{\nu}{\sigma_t}\right) \tag{2.23}$$

$$\sigma_t = \sqrt{\sigma_0^2 + 2\phi\nu t}. \tag{2.24}$$

Thus, the variation in the standard deviation of vorticity is given by (2.24), where σ_0 is the standard deviation at a user-defined initial time. It is worth noting that the rate

https://doi.org/10.1017/jfm.2017.815 Published online by Cambridge University Press

of change of standard deviation is independent of the peak vorticity ω_m, and depends only on the kinematic viscosity and instantaneous standard deviation.

In the above derivation, the conservation principle is applied to the entire system, comprising of the internal disk plus the adjoining fluid region. In contrast, equations (2.15) and (2.18) refer to the viscous effects on the internal fluid disk only. This conservation principle is applied considering the validity of Newton's law that the total angular momentum of a system remains unaltered under the action of torques internal to the system. As the viscous torque retards the internal disk, it has an equal and opposite influence on the surrounding fluid layer. The adjoining layer thus gains momentum, keeping the total momentum of the configuration constant.

Using the above result, (2.18) can be modified and solved for peak vorticity variation (2.26),

$$\frac{\partial \omega_{avg,t}}{\partial t} = -4\phi \frac{\nu \omega_{avg,t}}{(\sigma_0^2 + 2\phi\nu t)} \tag{2.25}$$

$$\omega_{avg,t} = \frac{\omega_{avg,0}}{\left[1 + \dfrac{2\phi\nu t}{\sigma_0^2}\right]^2} \quad \text{i.e. } \omega_{m,t} = \frac{\omega_{m,0}}{\left[1 + \dfrac{2\phi\nu t}{\sigma_0^2}\right]^2}. \tag{2.26a,b}$$

From (2.26) and (2.24) it can be seen that the maximum vorticity decreases as the square of the time whereas the standard deviation increases as the square root of time. Thus, the vorticity distribution inside the vortex can be written as

$$\omega(r, t) = \frac{\Gamma_0}{(\sigma_0^2 + 2\phi\nu t)} \mathrm{e}^{-(r/\sqrt{\sigma_0^2 + 2\phi\nu t})^2}, \tag{2.27}$$

where $\Gamma_0 = \pi\omega_{m,0}\sigma_0^2$. Using these values, we can find the circulation at any instant of time by computing the area integral of vorticity within a closed contour C around the vortex core:

$$\Gamma \propto \int \omega \, \mathrm{d}\psi = \pi\sigma^2\omega_m \tag{2.28}$$

$$\Gamma \propto \frac{\pi\sigma_0^4\omega_{m,0}}{(\sigma_0^2 + 2\phi\nu t)} = \frac{\Gamma_0}{\left(1 + \dfrac{2\phi\nu t}{\sigma_0^2}\right)}. \tag{2.29}$$

Thus, in the case of viscous fluids, the vortex circulation decreases with time. Although fluid viscosity results in loss of circulation, it is believed that in the absence of body forces the total hydrodynamic impulse imparted to a system cannot change (Batchelor 2000). Therefore, the total impulse given by (2.30), where a is a ring radius, must be conserved:

$$I \propto \Gamma a^2. \tag{2.30}$$

Considering the variation in circulation given by (2.29), temporal variations in vortex spacing a can be derived as

$$a = a_0 \sqrt{1 + \frac{2\phi\nu t}{\sigma_0^2}}. \tag{2.31}$$

https://doi.org/10.1017/jfm.2017.815 Published online by Cambridge University Press

For a vortex ring defined by (2.27), the propagation velocity at a point on the ring axis can be calculated using Biot–Savart's law in polar coordinates as

$$\boldsymbol{V}(x, y, z) = \frac{\Gamma}{4\pi} \int_0^{2\pi} \frac{r\,\mathrm{d}\boldsymbol{\theta} \times \boldsymbol{r}}{|\boldsymbol{r}|^3}. \tag{2.32}$$

Using Saffman's equation for viscous fluids (1.2) and applying it to our vorticity profile, we calculate the vortex propagation velocity at the leading order, given by

$$V = \frac{\Gamma}{4\pi a}\left[\ln\left(\frac{8a}{\sigma}\right) - 0.558\right] = \frac{\Gamma_0}{4\pi a_0\left(1 + \dfrac{2\phi\nu t}{\sigma_0^2}\right)^{3/2}}\left\{\ln\left(\frac{8a_0}{\sigma_0}\right) - 0.558\right\}. \tag{2.33}$$

The above equation clearly shows that, for larger times t, circulation of the vortex reduces hyperbolically while the corresponding propagation velocity is proportional to $t^{-3/2}$. This decreasing velocity trend was first observed by Reynolds (1876). He attributed this to entrainment effects resulting in growing vortex size.

The above-derived equations can be written in non-dimensional form as

$$t^* = \frac{2\phi\nu t}{\sigma_0^2}, \quad \omega^* = \frac{\omega_{m,t}}{\omega_{m,0}} = \frac{1}{(1+t^*)^2}, \quad \sigma^* = \frac{\sigma_t}{\sigma_0} = \sqrt{1+t^*} \tag{2.34a–c}$$

$$a^* = \frac{a_t}{a_0} = \sqrt{1+t^*}, \quad \Gamma^* = \frac{\Gamma_t}{\Gamma_0} = \frac{1}{(1+t^*)}, \quad V^* = \frac{V_t}{V_0} = \frac{1}{(1+t^*)^{3/2}} \tag{2.35a–c}$$

These results are in good agreement with the equations proposed by Saffman (1970) and Reynolds (1876). However, these are somewhat different from those obtained by Maxworthy (1972). He attributed the loss of vorticity to the wake. Our equations are derived by considering the macroscopic aspects of vortex evolution and no reasoning is yet provided for the mechanism responsible for loss of circulation. A detailed reasoning towards circulation reduction will be provided in § 5. Moreover, these equations are derived considering the same fundamental assumptions as used by Maxworthy: (i) the vortex distribution is Gaussian and symmetric about the core centre; (ii) any changes in vorticity due to internal or external viscous effects are reflected instantaneously by an overall change in the vorticity distribution, and (iii) the total impulse of the vortex ring remains constant. These assumptions have been scrutinized in greater detail in § 5.

Though the results do not seem to bring any major advancement over the already available theory of Saffman, we would like to emphasize the importance of this model on a couple of fronts. Firstly, here we have approached the finite thickness vorticity diffusion problem using a completely new dimension which has enabled us to formulate a simple pseudo self-similar solution. This is a major advancement considering the complex non-self-similar mathematical solutions of such cases (§ 2.1). Secondly, while deriving long-term limits, for thick core vortex equations, Saffman (1970) explicitly solved for Hill's spherical vortex with a core size equal to half of the vortex spacing. Thus, his theory does not completely comply to cases with slenderness ratio less than unity. Saffman (1970) also reported this fact. Also, his model does not help us in determining the variation of core size and peak vorticity values, which are important vortex parameters. These are critically addressed in the current model. Although the current effort does not negate or disprove any of the

https://doi.org/10.1017/jfm.2017.815 Published online by Cambridge University Press

previous results, the elegant mathematical formulation of the problem in § 2 helps us to better understand its validity and scope. It also helps us to derive a transitional theory in § 5.

We also realize that the current model is not a controlled approximation of the vorticity equation and has been solved using an unconventional approach. Thus, some important aspects must be remembered. Firstly, the solution has been obtained for an isodensity, isoviscosity fluid. Thus, the solution is applicable only to non-buoyant cases. Further, this approach is derived based on a Gaussian axisymmetric vorticity profile, and any deviation from these assumptions will affect the accuracy of the model. Therefore, the current model may not work effectively for extremely thin rings or point vortices, where the vorticity distribution may be highly localized. Also, it may perform unsatisfactorily for very thick cores due to the significant skewness in their Gaussian profiles. Lastly, the effects of any vortex instabilities have not been considered.

There have been many exhaustive studies on vortex evolution where the effects of convective velocity on vortex geometry have also been considered (Fraenkel 1972). In practical cases, the local flow induced by vortex rings consists of not only circular vorticity fields, but also the self-induced straining field resulting from translational motion. This straining field manifests itself at second order and deforms the core into an ellipse elongated in the propagating direction (Fraenkel 1972; Dyson 1893). The relative effect of the straining field is dependent on the fluid properties, with viscosity playing an important part in selecting the realized vorticity profile. Quadrupole components operate only at $O(\nu/\Gamma)$, leading to an elliptic vorticity distribution where the major axis of the ellipse is inclined at 45° to the principal axis of the external strain (Fukumoto & Moffatt 2000; Fukumoto & Kaplanski 2008).

3. Experimental details

3.1. *Experimental set-up*

Experiments have been performed to provide supportive evidence for the claims related to the current theoretical study. A schematic of the experimental set-up is shown in figure 4. It consists of a cubic test section of dimensions 140 mm × 140 mm × 500 mm, with an opening at the top and transparent glass walls on all four sides. Optical accessibility is maintained to facilitate sophisticated imaging by techniques such as shadowgraphy, particle image velocimetry (PIV) and laser induced fluorescence (LIF).

The vortex ring is introduced into the fluid domain from the top through a centrally located nozzle of diameter 15 mm. The fluid inlet was adjusted with the help of a solenoid valve connected to a LabVIEW-assisted computerized system. This ensured accurate control and proper synchronization of the experimental set-up. Vortex parameters are controlled by changing the valve opening time t_0. The maximum valve opening time is limited by the formation number (L/D_n) (Gharib *et al.* 1998).

3.2. *Imaging techniques*

Flow behaviour was visualized using high-speed LIF and PIV. The LIF technique was used here to capture the spatial properties of vortex structures. Here a CNI Optoelectronics continuous laser of 3 watt power with an emission wavelength of 523 nm was used to make a light sheet of 1 mm thickness. The injected fluid was mixed with Rhodamine B dye for visualization. A high-resolution camera

https://doi.org/10.1017/jfm.2017.815 Published online by Cambridge University Press

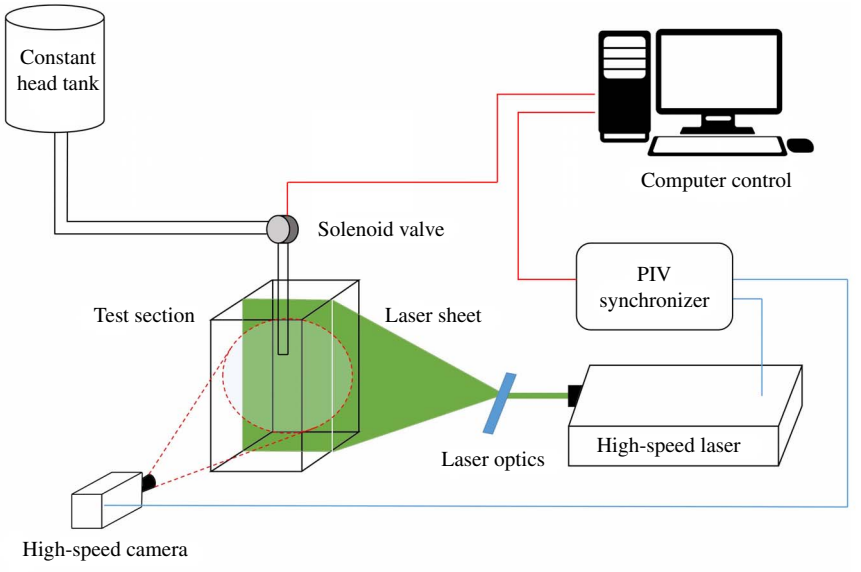


FIGURE 4. (Colour online) Experimental set-up with imaging modalities.

(Nikon D7200) was used to capture images at a resolution of 6000 × 4000 pixels. Here the vortex formation, evolution and entrainment effects were clearly visible. LIF images have a higher resolution than PIV images, and thus LIF is the most sought after technique for studying vortex structures (Johari & Fang 1997; Bond & Johari 2010). Although LIF offers a higher resolution and crisp images, often the diffusion coefficient of the dye is less than the diffusion of vorticity (Maxworthy 1972). Therefore, LIF images may not provide an accurate interpretation of the vortex size and its spatiotemporal growth.

Dynamical properties of the vortex ring, such as velocity, vorticity distribution and circulation, were captured using a high-speed LaVision PIV system. Hollow borosilicate glass spheres of density 1.1 g cm^{-3} and mean diameter 9–13 μm were used as seeding particles. A high-speed dual-pulsed Nd:YLF Photonics laser was used to generate a thin laser sheet of thickness 1 mm using a divergent sheet-making optics and telescopic lens arrangement. The LaVision Davis 8.2 software was used to process 2D displacement vectors at the centre plane. Imaging was performed using a Photron model SA-5 camera positioned normal to the image plane (figure 4) at a distance of 1 m. Images were captured at 500 Hz with a spatial resolution of 1024 × 1024 pixels. The time interval between two successive lasers pulses was kept at 600 ns. This interval was arrived at in accordance with the optimal shift of particles within two frames (Keane & Adrian 1990). The experimental configuration enabled us to capture a field of view of 140 mm × 140 mm.

Postprocessing was performed using an interrogation window size of 12 × 12 with 50 % overlap. The seeding density was adjusted such that the maximum number of particles per interrogation window was limited to 10 (Raffel *et al.* 2013). This processing condition resulted in a field measurement of 171 × 171 velocity vectors with an optimized spatial resolution of 0.789 × 0.789 mm. Such a high resolution was necessary to accurately capture the vorticity distribution inside the core.

https://doi.org/10.1017/jfm.2017.815 Published online by Cambridge University Press

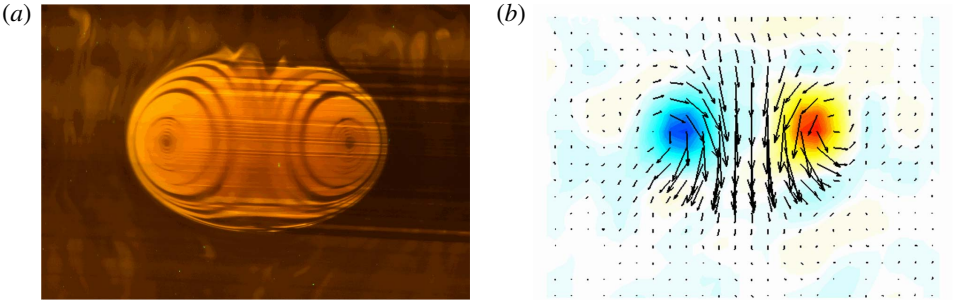


FIGURE 5. (Colour online) Experimental picture: (*a*) LIF of a fully developed vortex ring and (*b*) the corresponding PIV contour.

3.3. *Methodologies*

Data files generated from PIV were imported into MATLAB for data processing. Azimuthal vorticity (ω) values were calculated using the central-difference scheme as below:

$$\omega_{x,y} = \frac{V_{x+1} - V_{x-1}}{2\Delta y} - \frac{U_{y+1} - U_{y-1}}{2\Delta y}. \tag{3.1}$$

Vortex cores were located ($X1$, $Y1$) and ($X2$, $Y2$) by tracking maximum and minimum values of azimuthal vorticity (ω) in the entire domain. Using these values, the vortex spacing $2a$ at any instant was extracted by calculating the geometric distance between the core centres:

$$2a = \sqrt{(X1 - X2)^2 + (Y1 - Y2)^2}. \tag{3.2}$$

For the majority of the calculations, the vertical position of the vortex cores of both clockwise and anticlockwise vortices coincided with each other, which guaranteed a linear vertical translation of the vortex rings. The displacement L_p was then calculated by taking the absolute difference between the 'Y' locations of vortex core and the location of the nozzle exit.

$$L_p = |Y1 - Y_n|. \tag{3.3}$$

The circulation was obtained by performing area integration of the vorticity fields within a fixed closed circular contour of radius = 5 mm centred at the location of ω_m. The vorticity distribution along a horizontal line passing through the vortex core was used for calculating the interpolated value of the standard deviation for the Gaussian profile. This value was calculated in the direction of the ring axis. These methodologies have been kept consistent throughout our study.

3.4. *Experimental conditions*

For our experimental set-up, stroke length L can be defined as a product of outlet velocity V_0 and valve opening time t_0 ($L = V_0 t_0$). Since V_0 is governed by the pressure head inside the tank, which remains almost constant, we change the inlet conditions for experiments by altering the value of the valve opening time t_0. Using this method, we have performed studies for a wide range of inlet conditions. The approximate value of the circulation imparted was calculated from PIV data at the beginning of the evolution period. Care was taken to keep the inlet Reynolds number (Re_0) and L/D_n ratio within limits.

https://doi.org/10.1017/jfm.2017.815 Published online by Cambridge University Press

Case Glycerol soln.	Viscosity $\nu \times 10^{-7}$ (m^2 s^{-1})	Valve times t_0 (ms)	Case name	Out. velocity V_0 (m s^{-1})	FN $(V_0 t_0/D_n)$	Γ_i (cm^2 s^{-1})	Re_0 (Γ_0/ν)
Case 1: 60 % by wt.	9	45	C1-45	0.5	1.5	120	1332
	9	60	C1-60	0.5	2.0	112	1238
Case 2: 75 % by wt.	25	45	C2-45	0.5	1.5	100	397
	25	60	C2-60	0.5	2.0	98	392
Case 3: 90 % by wt.	150	45	C3-45	0.5	1.5	115	77

TABLE 1. Experimental and operating conditions.

Experiments were conducted using aqueous glycerol solution at three different concentrations and different valve opening times. The density of solution remained roughly in the range 1.05–1.15 g cm^{-3} while the kinematic viscosity varied from 9 to 180 centipoise mPa^{-1} s^{-1}. Based on the vortex circulation, the Reynolds numbers obtained varied in the range from 50 to 1500. Further details of the operating conditions have been given in table 1. Each case was repeated three times to assure repeatability.

4. Results

4.1. *Preliminary observations*

Figure 6 shows the variation in vorticity distribution over time. Initially, the injected fluid curls around the nozzle edge, leading to vortex formation, as visible in figure 7(*a*,*b*). During this period (t_f), the vortex entrains surrounding fluid into the ring, leading to a considerable and sharp increase in peak vorticity (ω_m), ring size ($2a$) and circulation (Γ), as shown in figure 8(*b–d*). Figure 7(*a–c*) shows LIF images of the initial vortex formation period from injection to pinch off. This vortex is underdeveloped with sharp and asymmetric variations in vorticity. This transient phase ends with closing of the nozzle valve after the vortex has propagated a distance of approximately 2–3 times the nozzle diameter (figure 8*a*). This termination of the development period is marked by a sudden drop in the circulation and vortex spacing, which is evident from figures 7 and 8. After this initial formation period, the vorticity gets distributed smoothly throughout the vortex core. The radial distribution of vorticity for experimental case C2-60 at different locations (L_p/D_n) is shown in figure 8(*f*). These stable vorticity variations closely mimic the Gaussian distribution (Weigand & Gharib 1997; Cater, Soria & Lim 1998). Parameters such as the maximum vorticity value and standard deviation σ depend on the inlet conditions and dynamics during the vortex formation phase t_f.

Beyond t_f, the vortex propagates in its self-induced field with predictable dynamics. Figure 7(*d–f*) show steady evolution of vortex rings. We have focused our attention on this developed regime, neglecting the initial transient effects.

Figure 8 shows the variation in vortex ring parameters with respect to time for the C2-60 case. Preliminary observations (figure 8*a*) show a linear trend in vortex translation with negligible acceleration. However, considerable exponential decay can

https://doi.org/10.1017/jfm.2017.815 Published online by Cambridge University Press

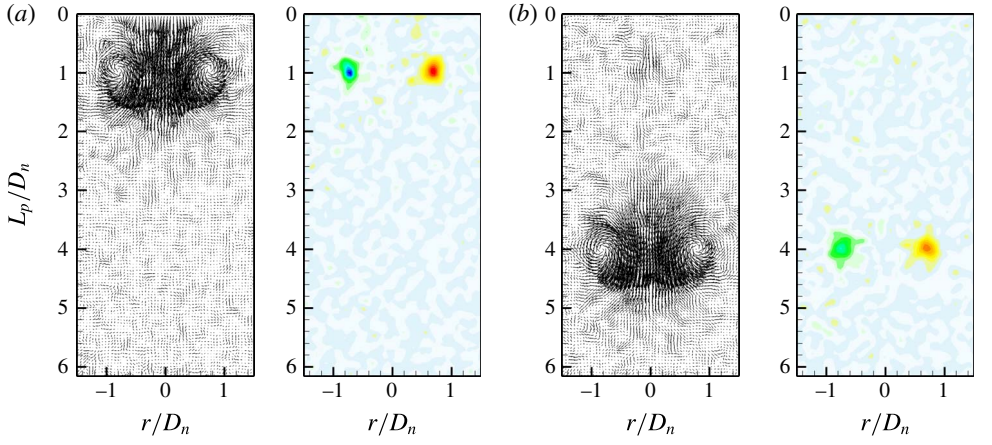


FIGURE 6. (Colour online) PIV vector and vorticity contour plots for C2-60 at (*a*) $L_p/D_n = 1$ and (*b*) $L_p/D_n = 4$.

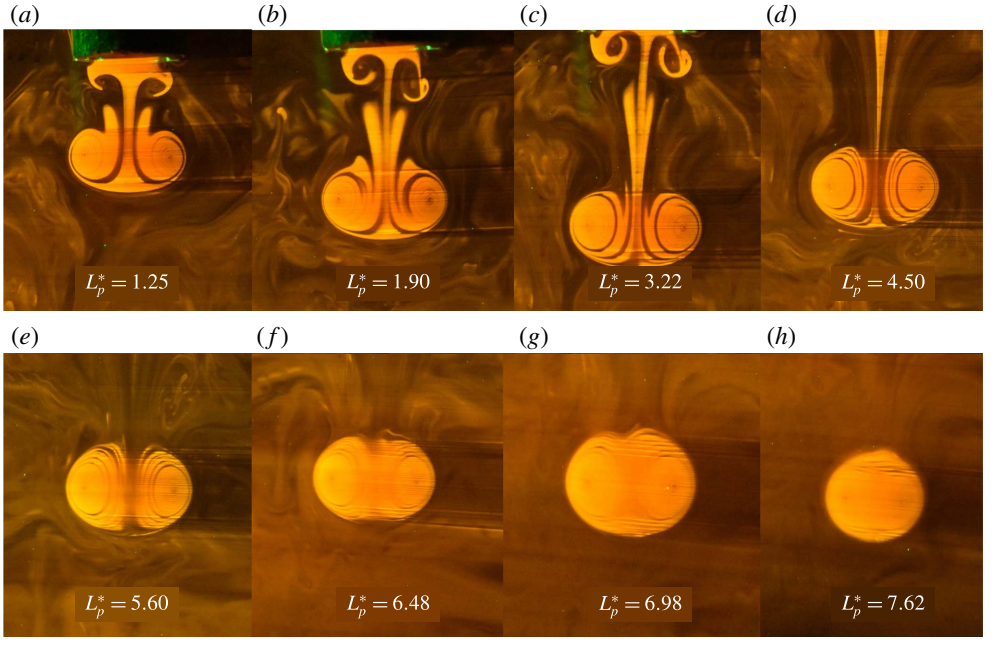


FIGURE 7. (Colour online) Flow visualization images of vortex ring at different positions during its propagation for C2-60.

be observed for the peak vorticity values (figure 8*b*). For the C2-60 case, the peak vorticity reduces by approximately 30 % in a short time span of 0.3 s. Contours shown in figure 6 offer greater insights into this phenomenon. A similar trend is seen in the variation of circulation (Γ) (figure 8*d*). This reduction of vorticity and circulation is attributed to viscous dissipation of the vorticity.

The decrease in maximum vorticity is complemented by a corresponding increase in the vorticity distribution. As the vortex propagates, it entrains the surrounding, initially

https://doi.org/10.1017/jfm.2017.815 Published online by Cambridge University Press

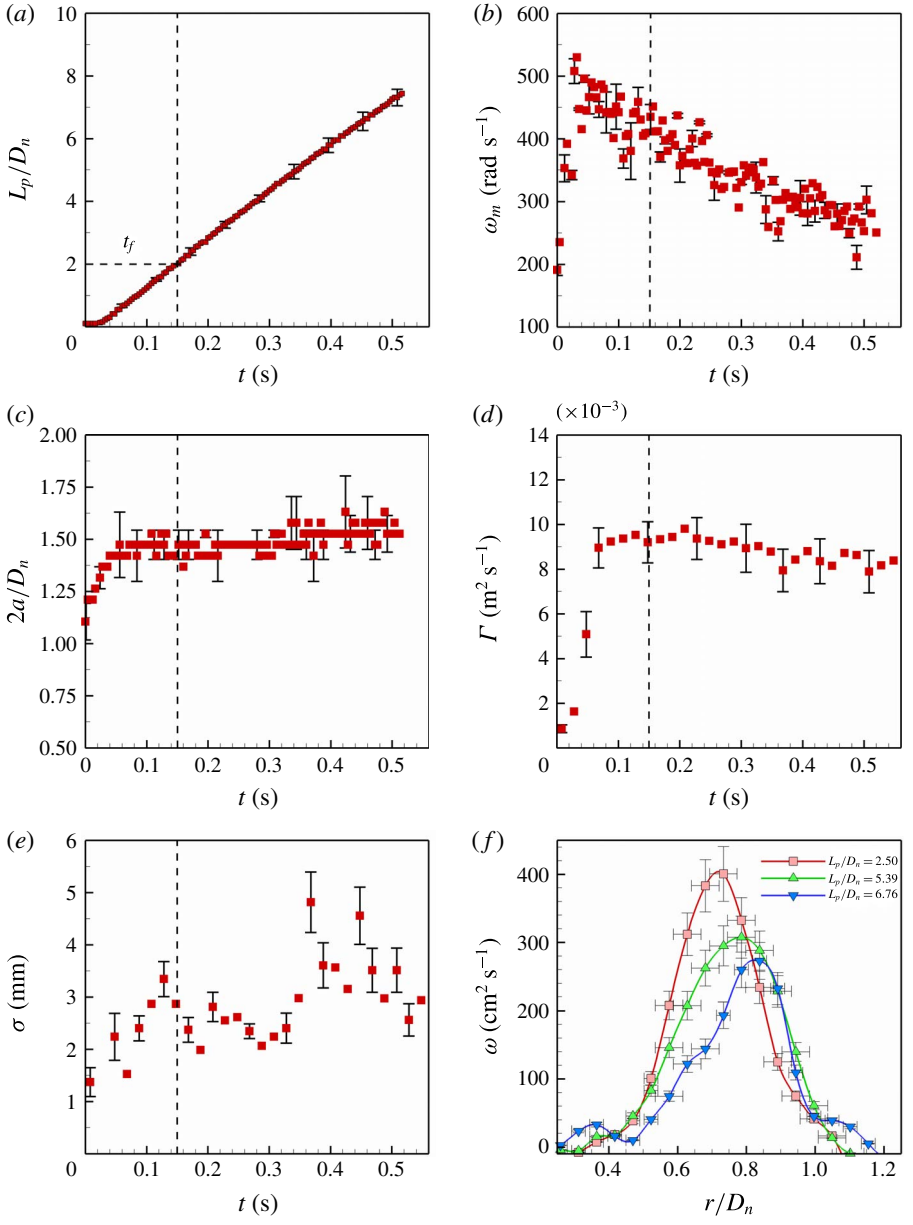


FIGURE 8. (Colour online) PIV obtained graphs of C2-60 for vortex parameters: (*a*) L_p/D_n versus t, (*b*) ω_m versus t, (*c*) $2a/D_n$ versus t, (*d*) Γ versus t, (*e*) σ versus t, (*f*) ω versus r/D_n.

irrotational fluid. This increases its bulk mass, sharing its vorticity in the process. Thus, the standard deviation σ of the Gaussian distribution increases with time, as shown in figure 8(*e*). These variations in the vorticity distribution are considered to be largely governed by viscous effects. Therefore, for inviscid fluids, vorticity does not decay and remains concentrated in thin cores. For such cases, the circulation remains conserved. In addition to vorticity dissipation, the ring radius a is also observed to increase. From figure 8(*c*), it can be seen that this increase is negligible initially.

https://doi.org/10.1017/jfm.2017.815 Published online by Cambridge University Press

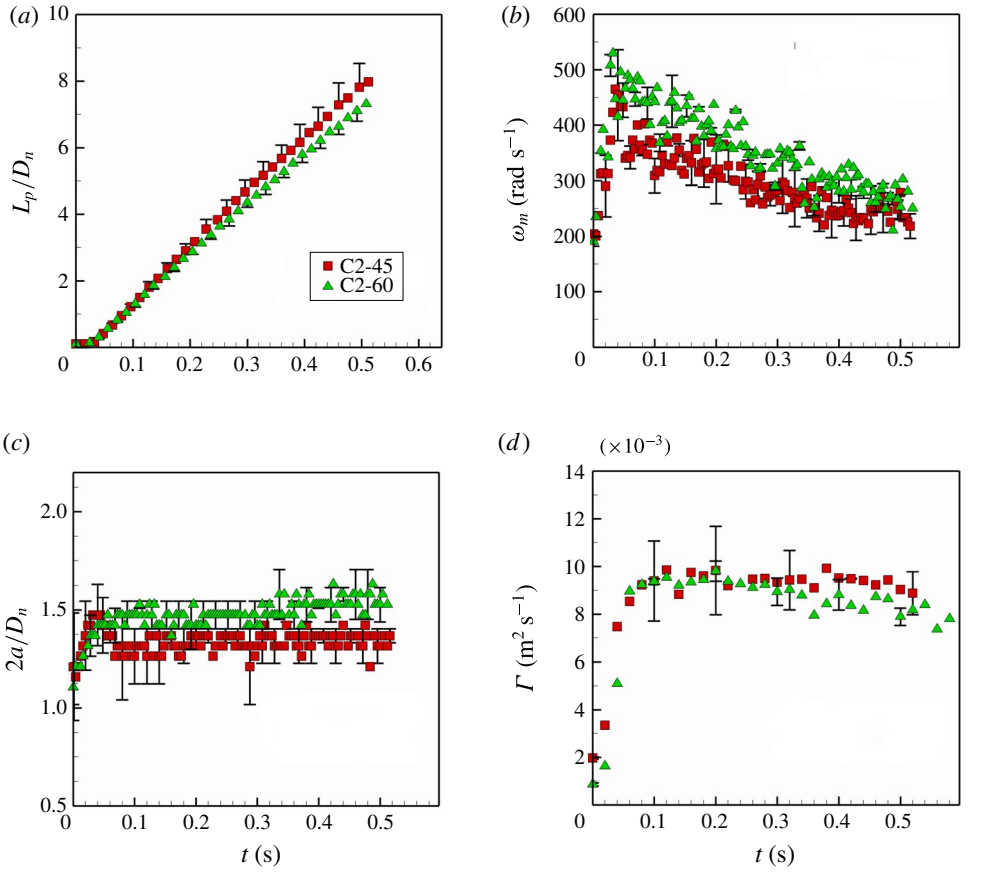


FIGURE 9. (Colour online) Comparison between C2-45 and C2-60: (*a*) L_p/D_n versus t, (*b*) ω_m versus t, (*c*) $2a/D_n$ versus t, (*d*) Γ versus t.

However, this rate increases as time progresses, and significant expansion effects are seen at larger times.

It is also important to note that all the variables except σ show high repeatability, with errors within 10 % of the mean. High scatter is seen in the graph of σ. This is due to the limited resolution of PIV, where σ values are comparable with the least count of our vector resolution. Although figure 8 shows trends only for the C2-60 case, similar behaviour is observed for other test cases also. However, the quantitative aspects of these variations depend on the vortex geometry and fluid viscosity. Greater insights into these aspects are provided in § 5.

4.2. *Comparison between cases*

Figure 9 shows the variation in vortex parameters during their evolution for cases C2-45 and C2-60. The qualitative nature of the plots for both cases are almost similar. However, it is interesting to see that the vortex propagation velocity for C2-45 is marginally higher than C2-60. This may compel us to believe that C2-60 would carry lower vorticity values than C2-45. This is not evident from the plots (figure 9*b*). On the contrary, ω_{max} values for C2-60 are significantly higher than C2-45. Moreover, vortex circulation values as shown in figure 9(*d*) are almost similar for both cases.

https://doi.org/10.1017/jfm.2017.815 Published online by Cambridge University Press

The observed phenomenon can only be explained provided the value of the standard deviation σ for C2-60 is lower than for C1-45. However, this cannot be validated using our PIV data, due to high scatter. It can also be seen that the vortex spacing for C2-45 is consistently lower than for C2-60. This indicates a positive correlation between the vortex spacing and formation number ((L/D_n) or $(V_0 t_0/D_n)$). This increased spacing may account for the lower translational velocity of C2-60. Such anomalous behaviour is also observed for the C1-45 and C1-60 cases.

In addition, it was most interesting to observe that the translational velocity for C3-45 was considerably higher than for C2-45, even though its peak vorticity values were significantly lower and the spacing $2a$ was higher than for C2-45. Insights into such counterintuitive behaviour are not addressed here and could form a topic of an altogether independent study. However, since this behaviour depends on vortex formation, we believe that it will be reflected in the vortex parameters (post-formation). It is expected that the dynamics of vortex evolution will not be affected provided that the vorticity variation is stable and follows a Gaussian distribution.

4.3. *Comparison with theoretical predictions*

Experimental results are used to validate the theoretical predictions offered in § 2. In view of this, we use optimization techniques to find a parameter that will best fit the vortex variables. MATLAB code was written to perform deterministic optimization by implementing the 'gradient inversion' technique, the details of which are given in appendix A. Using this technique, we calculate the best-fit parameter β on a 60 % cropped experimental dataset of ω_m, where β stands for

$$\beta = \frac{2\phi\nu}{\sigma_0^2}. \tag{4.1}$$

Consequent to evaluating the best-fit parameter using any one variable (here ω_m), we use this value to predict the variations in the other vortex parameters. We believe that the high accuracy of our predictions with other observed values should act as validators for the theory.

Using this approach, we have compared the measured values of vortex position (L_p), peak vorticity (ω_m), sigma (σ), circulation (Γ) and vortex spacing ($2a$) with the values obtained using the theoretical equations (§ 2). The variations in these parameters along with the best-fit predictions are shown in figures 10 and 11.

It is worth mentioning that the value of β obtained by the best fit of maximum vorticity leads to a near accurate estimate of the variation in the other parameters also. Even though good accuracy is obtained for the prediction of Γ, high scatter is seen for σ (not shown here) for the reasons explained in § 4.1. It is also visible that the theoretical predictions for vortex position are always lower than the experimentally observed values. Thus, it can be inferred that our theory underpredicts propagation velocities compared to experimentally observed values. Similarly, figure 10(c) also shows marginal overprediction for the vortex spacing ($2a$). A detailed explanation regarding this behaviour is provided in § 5.2.

All experimental cases have been compiled into combined plots (figure 12) using the non-dimensional form of (2.34) and (2.35). Thus, it can be seen that our theoretical model closely predicts vortex evolution in viscous fluids.

https://doi.org/10.1017/jfm.2017.815 Published online by Cambridge University Press

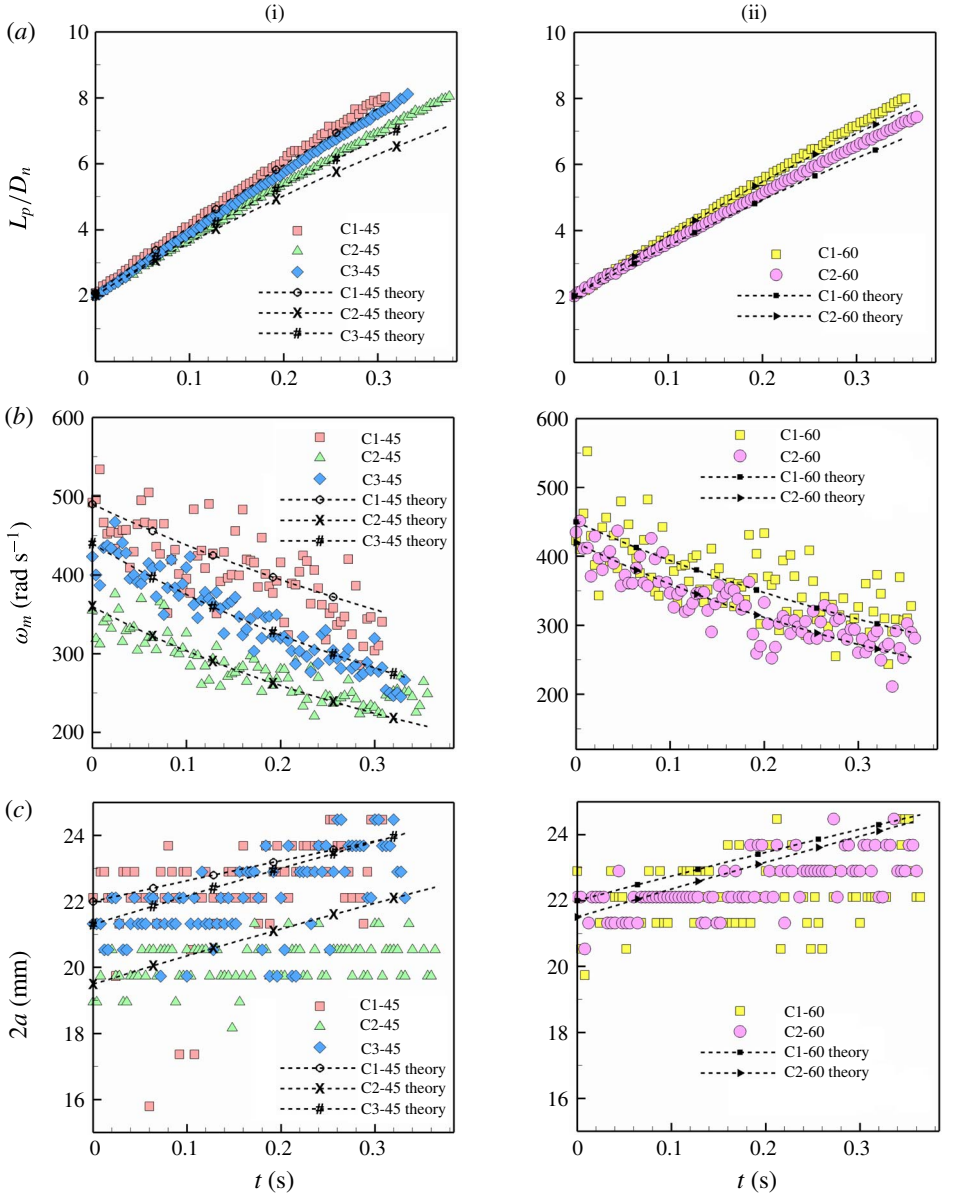


FIGURE 10. (Colour online) Validation of experimental results with theory: (*a*) L_p/D_n versus t, (*b*) ω_m versus t, (*c*) $2a$ versus t.

4.4. *Comparison with available literature*

In order to test the effectiveness of our proposed theory, we have performed comparative studies on already existing experimental, numerical and analytical results. Figure 13(*a*) shows the variation in experimental and theoretical values of vortex spacing $2a$ for our case C2-60 and the respective predictions resulting from the analytical studies of Maxworthy (1972) and Fukumoto & Moffatt (2000) using (2.34) and (2.35). Corresponding data for the variation in circulation are also provided (figure 13*b*). We see that the current theory provides a better match for observed

https://doi.org/10.1017/jfm.2017.815 Published online by Cambridge University Press

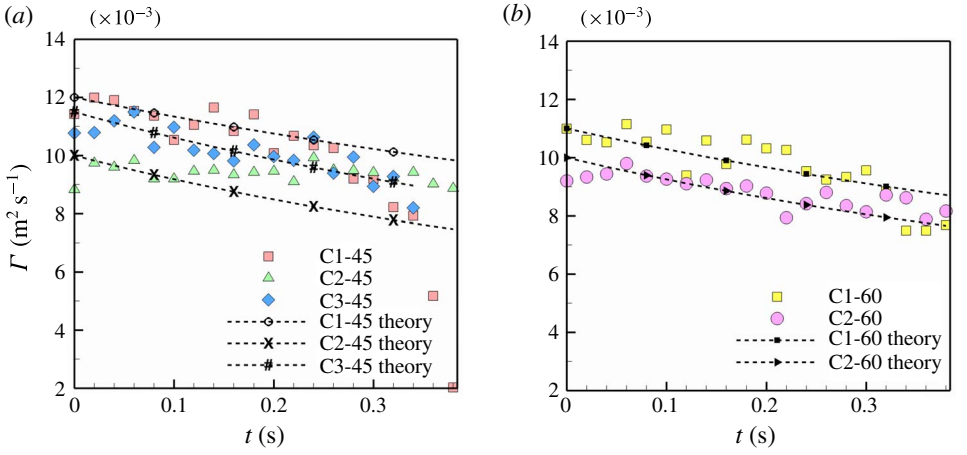


FIGURE 11. (Colour online) Validation of experimental results with theory: Γ versus t.

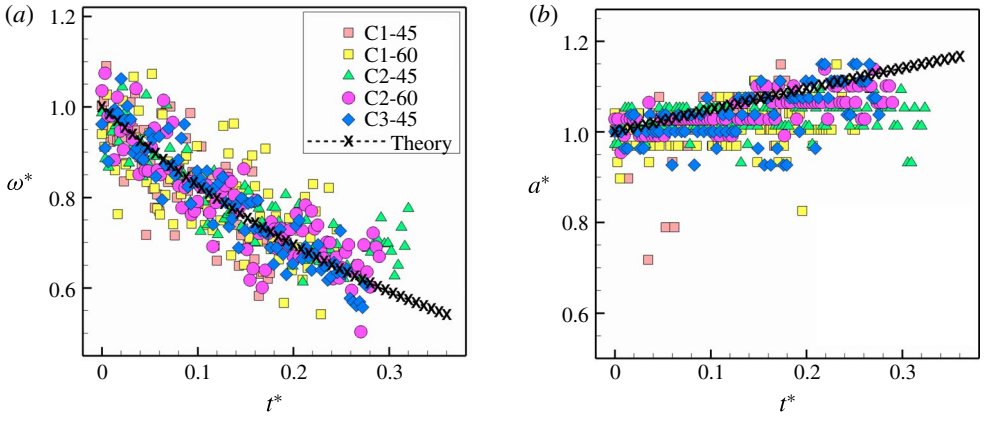


FIGURE 12. (Colour online) Non-dimensional forms of graphs for (*a*) ω^* versus t^* and (*b*) a^* versus t^*.

values for the variation in circulation, whereas Maxworthy's formula gives a better fit for the variation in vortex spacing $2a$. In addition, the linear formula used by Fukumoto is seen to underpredict the expansion for C2-60.

Figure 13(*c*) shows the variation in peak vorticity values for C2-60. It is interesting to note that the predictions from the Lamb–Oseen equation of vorticity (1.1) largely deviate from the observed values. This highlights the limited applicability of the Lamb–Oseen equation to short-time asymptotes only. In figure 13(*d*), we have used the experimental data of Weigand & Gharib (1997) to perform a comparative assessment of current theory with Maxworthy's model. Moving forward, we have also tried to apply our theory to the DNS results of Archer, Thomas & Coleman (2008). Plots in figure 14 show the variation in non-dimensional forms of core radius and translational velocity for $Re = 5500$ and slenderness ratio ($r_c/a = 0.4$). Using the best-fit approach, it can be seen that the proposed theory offers a better prediction of the observed dynamics.

https://doi.org/10.1017/jfm.2017.815 Published online by Cambridge University Press

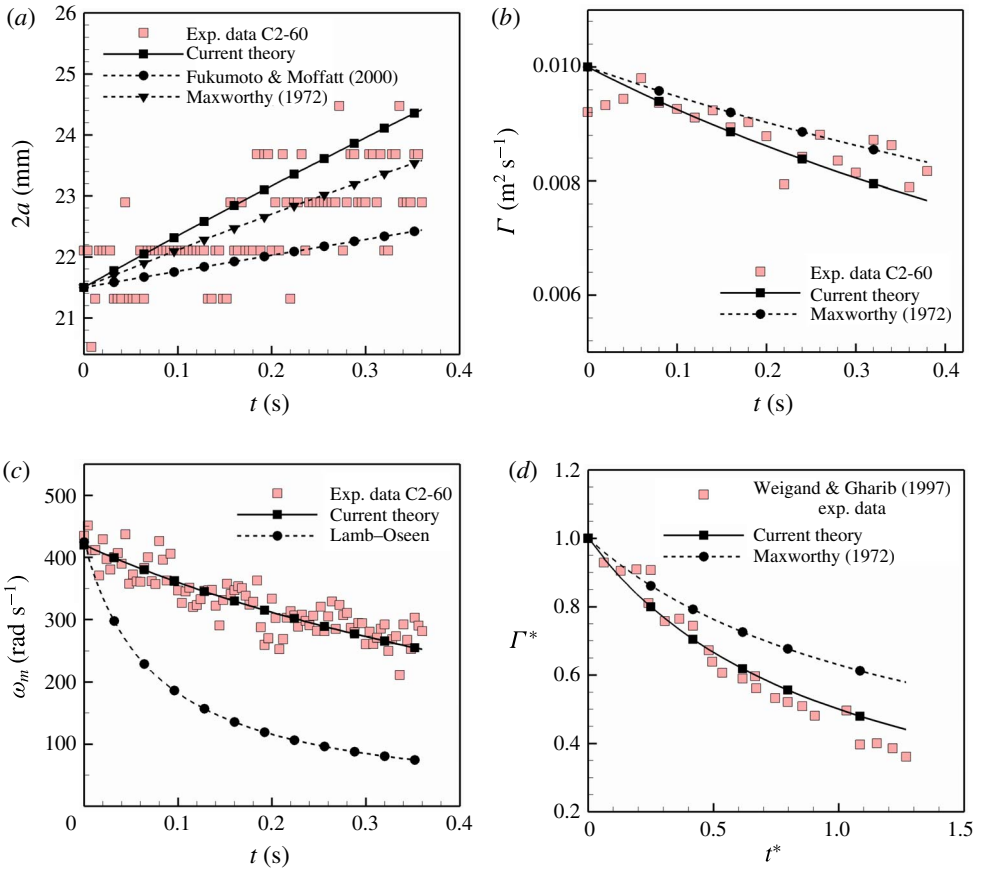


FIGURE 13. (Colour online) Comparison of experimental values with existing theories: (*a*) $2a$ versus t, (*b*) Γ versus t, (*c*) ω versus t, (*d*) comparison with the experimental data of Weigand & Gharib (1997).

It is necessary to mention that such studies have proved to be challenging. Many of the prior studies have rarely focused their attention on the vorticity distribution or precise core size, which forms an important parameter in our predictive theory. Moreover, the above comparisons have been conducted for practically thick vortex rings in the Reynolds number range 77–5500. Studies pertaining to thin rings have not been compared, primarily due to the scarcity of experimental results in this regime.

However, short asymptotic studies have proposed relations for the vortex propagation velocity which carry a completely different functional relationship with time. Saffman's equation claims a dependence relation of $-\log(\nu t)$, which is different from the relation $t^{-3/2}$ as concluded by current theory. Thus, we believe that the theory, in its current form, offers good insights into the medium–large-time regimes of vortex lifetimes, although it performs unsatisfactorily in the lower asymptotic limits. This subject is further discussed in § 5.

4.5. *Interpretations from the derived values of* β, k_1

Using the best-fit value of β for each case, combined with measured values of σ_0 and ν, we have calculated the averaging parameter ϕ, and thereby k_1 using the relation

https://doi.org/10.1017/jfm.2017.815 Published online by Cambridge University Press

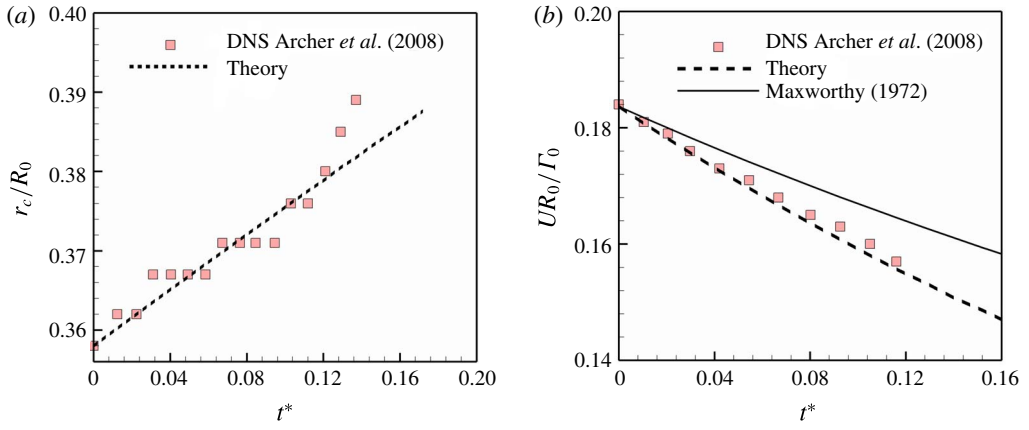


FIGURE 14. (Colour online) Fitting of our theory into the DNS data of Archer *et al.* (2008): (*a*) core size versus time, and (*b*) velocity versus time.

Case name	*Re*	β	ϕ	k_1
Archer *et al.* (2008) DNS	5500	—	0.5047	0.8485
C1-45	1332	0.5769	0.1755	0.7463
C1-60	1239	0.6887	0.2989	0.7810
C2-45	0397	0.8884	0.1472	0.7389
C2-60	0392	0.8045	0.1018	0.7287
C3-45	0077	0.8302	0.0215	0.7113

TABLE 2. Results table with parameter values for each case.

(2.19). These results are compiled in table 2. β is the only adjustable parameter in our theoretical model. Errors in β are sensitive to errors in the measurement of ω_m and the standard deviation σ (4.1). Considering the PIV resolution, the net accumulated error in β is approximately 10 %–12 %. Since ϕ is highly sensitive to changes in k_1 (2.19), the net error in k_1 translates to not more than 2 %–3 %.

Note that the value of β is obtained from curve fitting, and no mathematical relations have been provided. Similarly, our mathematical model did not specify the vortex core parameter k_1 that is to be used. This is because we believe that the vortex core parameter that is to be used for proper averaging is a complex function of vorticity distribution and fluid properties which is non-trivial to guess beforehand and would require separate dedicated efforts. Nevertheless, our approach provides important insights. It is observed (table 2) that the value of $k_1 > 0.707$ for our test cases, and approaches $(1/\sqrt{2})$ for decreasing Reynolds numbers. In case of low-Reynolds-number vortex rings, which have considerably thick vortex cores (vorticity distribution extending up to centreline, as in the fat-limit case of Hill's spherical vortex (Maxworthy 1972; Hill 1894)), we see that our theory predicts a k_1 value that is consistent with the available literature. In such cases, the core size ϵ will be given by $(k_1\sigma) \approx (k_1 \times a) = (a/\sqrt{2})$, which equals the proposed value of slenderness ratio for Hill's spherical vortex. Thus, our model seamlessly integrates with established theories.

https://doi.org/10.1017/jfm.2017.815 Published online by Cambridge University Press

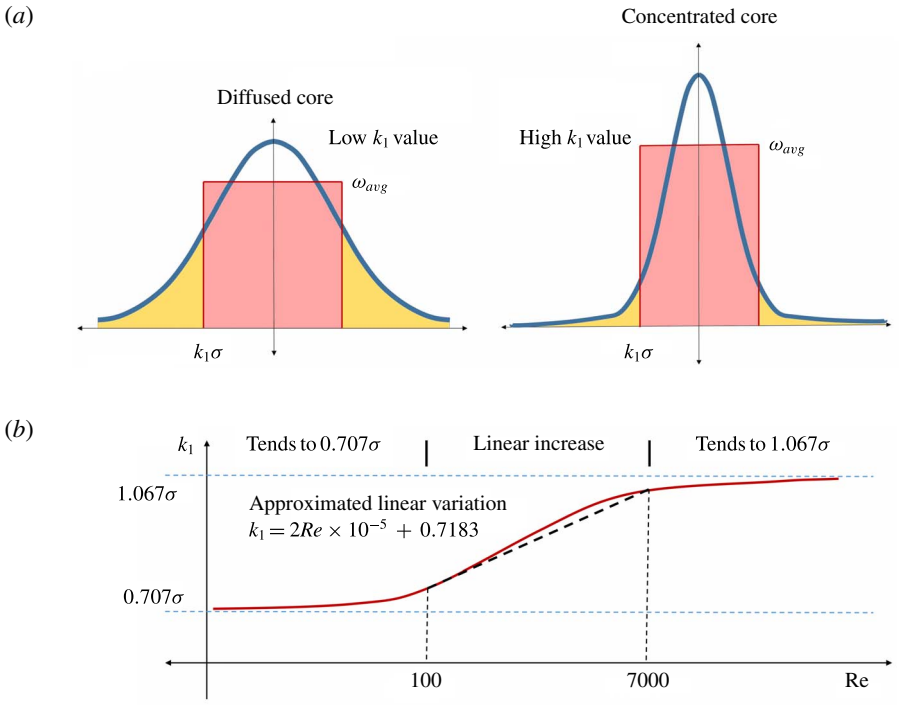


FIGURE 15. (Colour online) (*a*) Schematic showing the physical importance of the vorticity profile on the selection of the k_1 values. (*b*) Approximate variation in k_1 values w.r.t. Reynolds number.

Although the best-fit approach provides validation for our proposed theory, understanding the nature of variation in k_1 is necessary to transform it into a predictive and deterministic tool.

The variation in k_1 can be best analysed by understanding the physical role it plays in deriving the theory in § 2. k_1 is taken to be the radius of a hypothetical disc with constant average vorticity which best mimics the vorticity diffusion (figure 15*a*). Under this assumption, internal viscous interactions are neglected, thereby reducing the problem to that of external viscous diffusion only. Further, it can be intuitively understood that a core with high circulation will largely behave as a solid disc with negligible internal dissipation compared to external dissipative effects. Thus, Reynolds number plays a significant role in realizing k_1 values.

Our observations provide us with a lower bound of k_1 which approaches $(1/\sqrt{2})$ as $Re \to \infty$, which makes $\phi \to 0$ and results in negligible relative vorticity diffusion, as can be seen in (2.24). On the other end, as $Re \to \infty$, we predict that the value of k_1 should be such that it maximizes ϕ, leading to the maximum relative viscous dissipation. Using trial and error methods, we arrive at a value approximately equal to 1.067. This forms the higher asymptotic limit of k_1. Thus, the variation in k_1 with respect to Reynolds number can be best described by a curve as shown in figure 15(*b*).

In the moderate Re range (100–10 000), variation in k_1 can be approximated to be linear. From our obtained values (table 2), this linear trend can be quantified by the following equation;

$$k_1 = 2Re \times 10^{-5} + 0.7183. \tag{4.2}$$

https://doi.org/10.1017/jfm.2017.815 Published online by Cambridge University Press

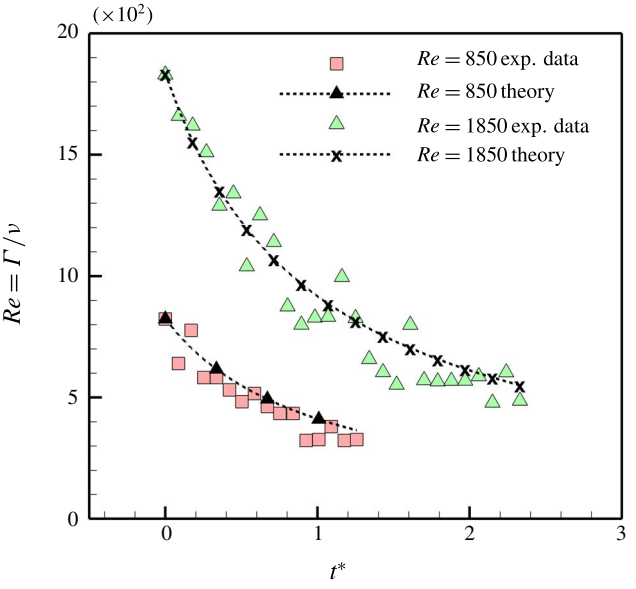


FIGURE 16. (Colour online) Fitting our theory on experimental data; non-dimensional circulation versus non-dimensional time.

Validation of the above equation has been attempted by comparing the same with the experimental results of Dziedzic & Leutheusser (1996). The theoretical trend shown in figure 16, obtained using (4.2), shows good agreement with the experimental values.

5. Discussions

5.1. *Differences between current theory and the Lamb–Oseen equation*

The classic equation for vorticity diffusion (1.1), widely accepted for understanding vortex evolution in viscous fluids, was given by Lamb–Oseen (Oseen 1910; Lamb 1932):

$$\omega(r, t) = \frac{\Gamma_0}{4\pi\nu t} \mathrm{e}^{-(r^2/4\nu t)}. \tag{5.1}$$

This equation was carefully derived assuming constant circulation. It is based on the argument that viscosity causes vorticity to diffuse out of the fixed contour. However, for smaller times, this effect is negligible. Thus, for short times, when the entire vorticity can be assumed to remain contained within the core, (1.1) has been accepted to provide good insights into vortex evolution. Also, it is explained that, for larger times, the vorticity diffuses and cancels itself at the vortex centreline, thus invalidating the assumption of constant circulation. Therefore, studies have shown that the Lamb–Oseen equation provides good insight into the dynamics of thin-core vortices at very short times, but it fails to explain the evolution of rings even with moderate slenderness ratio. These differences can be explained in the following way.

Consider a vortex monopole with the vorticity distribution given by (1.1), as shown in figure 2. For such a vortex the total circulation throughout the domain remains constant. This is a direct result of the constant circulation assumption used for

https://doi.org/10.1017/jfm.2017.815 Published online by Cambridge University Press

deriving (1.1)

$$\Gamma = \int_0^\infty \omega \, \mathrm{d}\psi = \text{const.} \tag{5.2}$$

Such viscous interactions are governed by the laws of conservation of angular momentum. For 2D cases, this results in the expression given below:

$$I = \int \omega \, \mathrm{d}I \propto \Gamma r^2 = \text{const.} \tag{5.3}$$

This suggests that circulation does not remain conserved even when calculated throughout the domain, but in fact decreases due to the addition of bulk fluid. Circulation reduction in a finite-size contour is thus a result of the superposition of two phenomena: (i) vorticity diffusion out of the contour and (ii) an increase in the vortex size.

We have used the above conservation principle to frame the proposed theory. No doubt the theory shows important differences with respect to that of Lamb–Oseen. It predicts a reduction in circulation values, which is indeed observed in our experiments.

5.2. *Insights into ring expansion and integration of short- and long-time behaviour*

Using our graphs (figures 10 and 11) depicting the variation in V^* versus t^*, it can be seen that the values obtained from our experimental studies show a variation with respect to theoretical predictions. Similar differences were reported by Maxworthy (1972). Moreover, it can be observed that this deviation between experimental values and theoretical predictions is relatively lower for low-*Re* cases, and increases with an increase in the vortex Reynolds number. It is also worthwhile mentioning that similar discrepancies are also noticeable in the variation of the vortex ring radius a^*. However, this mismatch seen in V^* and a^* with respect to t^* is not reflected in the graphs for the variation of ω^* or Γ^*. Thus, the observed phenomenon directs us to infer that the vorticity diffusion behaviour and consequent entrainment rates are largely governed by viscous effects only. However, the vortex translational velocity gradient and ring expansion are sensitive to Reynolds numbers.

This observed mismatch is somewhat logical if we consider the velocity–spacing coupling for vortex rings. For the Lamb–Oseen vortex (example), Saffman (1970) predicted the following velocity equation:

$$V = \frac{\Gamma_0}{4\pi a_0}\left[\ln\left(\frac{8a_0}{\sqrt{4\nu t}}\right) - 0.558\right]. \tag{5.4}$$

Thus, an overprediction related to vortex spacing a will reflect in lower theoretical values for the corresponding translational velocity. Fukumoto & Moffatt (2000) performed rigorous mathematical studies to understand the time evolution of the vortex spacing a and propagation velocity V. He obtained equations equivalent to (1.5) and (1.4). He attributed vortex ring expansion solely to viscous effects, which he put forward as linearly dependent on ν and independent of Γ. Though he was successful in gathering qualitative validation for his claims through comparison with already published results (Oshima 1972; Watanabe *et al.* 1995; Wakelin & Riley 1997), he could not provide any quantitative validation. For higher Reynolds numbers his proposed linear relation failed, and highly overestimated vortex ring expansion.

Experiments conducted by Weigand & Gharib (1997) show similar characteristics. They used a best-fit parameter in Saffman's equations (Saffman 1970) and observed

https://doi.org/10.1017/jfm.2017.815 Published online by Cambridge University Press

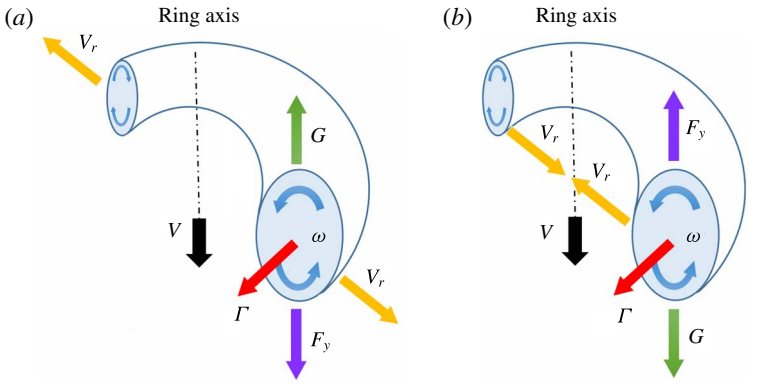


FIGURE 17. (Colour online) Forces on vortex rings: (*a*) during entrainment, (*b*) during detrainment.

that the translational velocity scales with (1.2) for shorter times, but shifts to (1.5) at larger times. This observation was also cross-validated by the numerical values of Stanaway *et al.* (1988). This aspect is studied in a whole new perspective in the recent work of Sullivan *et al.* (2008). In their exhaustive work, they compared their experimental data with published results. They concluded that, for thin vortex rings as generated in their experiments, vortex slowdown was primarily due to circulation reduction caused by hydrodynamic drag forces. However, they did not observe and account for the expected increase in core size and ring diameters.

Though these universal behaviours have been reported on numerous occasions, no physical insights into the transition of velocity profiles have been presented yet. Many comprehensive studies have elucidated the hydrodynamic mechanism governing the one-dimensional axial velocity variation of vortex rings. In contrast, relations for the variation in vortex spacing have been, most of the times, derived using dimensional analysis. Using dynamical equations of force balance, we try to explain this behaviour in more detail.

Variation in the vortex spacing $2a$ describes the radial displacement of the vorticity centre w.r.t. the axis of the vortex ring. For a vortex ring (figure 17) propagating in an isodensity fluid, and entraining mass on its way, it is under the influence of various forces: namely (i) the drag force opposing the vortex motion, (ii) the body force $\boldsymbol{F}_y$ acting in the axial direction, and (iii) the Magnus force $\boldsymbol{G}$. Of these, the effect of the drag force is negligible compared to the effect of increasing mass and spacing due to diffusion and circulation, respectively. For such vortex rings, the body force can be given by

$$\boldsymbol{F}_y \approx \boldsymbol{V}\frac{\mathrm{d}m}{\mathrm{d}t}. \tag{5.5}$$

Thus, for the rate of entrained mass to be positive, the body force acts in the direction of vortex motion. Using Newton's second law, we arrive at the dynamic equation for the vortex ring, given by

$$\boldsymbol{F}_y + \boldsymbol{G} = m\frac{\mathrm{d}\boldsymbol{V}}{\mathrm{d}t}. \tag{5.6}$$

However, for small values of mass and velocity variation, the right-hand side $\to 0$, and hence

$$\boldsymbol{F}_y = -\boldsymbol{G}. \tag{5.7}$$

https://doi.org/10.1017/jfm.2017.815 Published online by Cambridge University Press

The Magnus force $\boldsymbol{G}$ is opposite to the body force $\boldsymbol{F}_y$ and equal in magnitude. This force $\boldsymbol{G}$ over a vortex ring of radius a is mathematically given by

$$\boldsymbol{G} = (2\pi a)\rho(\boldsymbol{\Gamma} \times \boldsymbol{V}_r), \tag{5.8}$$

where $\boldsymbol{V}_r$ is the radial expansion velocity of the vortex ring, equal to $(\mathrm{d}a/\mathrm{d}t)$. From (5.5), (5.7) and (5.8) we arrive at an expression for the radial velocity, given by

$$|\boldsymbol{V}_r| = \frac{\mathrm{d}\boldsymbol{a}}{\mathrm{d}t} = \frac{1}{2\pi\rho a\Gamma} \times \left| \boldsymbol{V}\frac{\mathrm{d}m}{\mathrm{d}t} \right|. \tag{5.9}$$

A similar approach was used (Rayfield & Reif 1964; Sonin 2016) to study the dynamical properties of quantized charge-carrying vortex rings, moving in superfluid Helium at low temperatures, where the quantum of circulation was found to be equal to h/m, where h is Planck's constant and m is the mass of the Helium atom.

Thus, it can be observed that, when a vortex entrains fluid $(\mathrm{d}m/\mathrm{d}t > 0)$, the body force $\boldsymbol{F}_y$ acts in the direction of the vortex velocity and the radial velocity $\boldsymbol{V}_r$ points in the outward direction, leading to an increase in the ring diameter (vortex spacing in case of two dimensions). The opposite phenomenon is observed when detrainment occurs, as in case when the vortex penetrates a stratified medium. As the vortex penetrates through a higher density and higher viscosity fluid, viscous and buoyancy forces result in peeling of the vortex mass $(\mathrm{d}m/\mathrm{d}t < 0)$. In such cases, $\boldsymbol{F}_y$ acts opposite to the axial velocity and $\boldsymbol{V}_r$ should point inwards, leading to a collapse of the vortex rings.

The above approach can be extended further to understand the qualitative as well as quantitative aspects of vortex ring evolution. For a toroidal vortex ring with circular cross-section, as shown in figure 1, with core radius R, the mass of the ring can be given as

$$m = \rho(2\pi^2 aR^2). \tag{5.10}$$

Thus, for non-buoyant vortex rings, where the vortex density is unaltered due to entrainment effects, the rate of change of vortex mass is given by

$$\frac{\mathrm{d}m}{\mathrm{d}t} = 2\pi^2 \left[R^2\frac{\mathrm{d}a}{\mathrm{d}t} + 2aR\frac{\mathrm{d}R}{\mathrm{d}t} \right]. \tag{5.11}$$

Thus, equation (5.9) can be represented as

$$|\boldsymbol{V}_r| = \frac{\mathrm{d}a}{\mathrm{d}t} = \frac{1}{2\pi\rho a\Gamma}|\boldsymbol{V}|2\pi^2\rho \left[R^2\frac{\mathrm{d}a}{\mathrm{d}t} + 2aR\frac{\mathrm{d}R}{\mathrm{d}t} \right]. \tag{5.12}$$

After some manipulations, we arrive at a simplified implicit relation given by

$$\frac{\mathrm{d}a}{\mathrm{d}t} = \frac{2\pi R|\boldsymbol{V}|}{\Gamma\left\{1 - \dfrac{\pi|\boldsymbol{V}|R^2}{\Gamma a}\right\}}\frac{\mathrm{d}R}{\mathrm{d}t}. \tag{5.13}$$

However, for vortex rings, with the simplifying assumption that the entire circulation is distributed evenly in a finite core of radius R, the centreline velocity can be given by $|\boldsymbol{V}| = (\Gamma/4\pi a)$. This simplifies the above equation to give

$$\frac{\mathrm{d}a}{\mathrm{d}t} = \frac{2\left(\dfrac{R}{a}\right)}{\left\{4 - \left(\dfrac{R}{a}\right)^2\right\}}\frac{\mathrm{d}R}{\mathrm{d}t}. \tag{5.14}$$

https://doi.org/10.1017/jfm.2017.815 Published online by Cambridge University Press

If we consider the vortex core radius $R = \xi\sigma$, where ξ is a numerical constant determining the extent of the vortex core and σ is the standard deviation of the Gaussian vorticity distribution as shown in figure 3, we can write from our result (2.24)

$$\frac{\mathrm{d}R}{\mathrm{d}t} = \xi\frac{\mathrm{d}\sigma}{\mathrm{d}t} = \xi\frac{\left(\dfrac{2\phi\nu}{\sigma_0}\right)}{2\sqrt{1+\dfrac{2\phi\nu t}{\sigma_0^2}}}. \tag{5.15}$$

Substituting this in (5.14), we get

$$\frac{\mathrm{d}a}{\mathrm{d}t} = \frac{\left(\dfrac{\xi\sigma}{2a}\right)}{\left\{1-\dfrac{(\xi\sigma)^2}{4a^2}\right\}}\frac{\mathrm{d}R}{\mathrm{d}t} = \frac{\left(\dfrac{\xi\sigma}{2a}\right)}{\left\{1-\dfrac{(\xi\sigma)^2}{4a^2}\right\}} \times \xi\frac{\left(\dfrac{2\phi\nu}{\sigma_0}\right)}{2\sqrt{1+\dfrac{2\phi\nu t}{\sigma_0^2}}}, \tag{5.16}$$

where, substituting the relation for σ gives us

$$\frac{\mathrm{d}a}{\mathrm{d}t} = \frac{\dfrac{\xi\sigma_0\sqrt{1+\beta t}}{2a}}{\left\{1-\dfrac{\xi^2\sigma_0^2\sqrt{1+\beta t}^2}{4a^2}\right\}} \times \xi\frac{\left(\dfrac{2\phi\nu}{\sigma_0}\right)}{2\sqrt{1+\beta t}}. \tag{5.17}$$

Here β is a temporary variable given by $(2\phi\nu/\sigma_0^2)$. After cancellation of common terms, the above equation reduces to

$$\frac{\mathrm{d}a}{\mathrm{d}t} = \frac{\left(\dfrac{\xi^2\phi\nu}{2a}\right)}{\left\{1-\dfrac{\xi^2\sigma_0^2\sqrt{1+\beta t}^2}{4a^2}\right\}} = \frac{\phi\nu}{\left\{\dfrac{2a}{\xi^2}-\dfrac{(\sigma_0^2+2\phi\nu t)}{2a}\right\}}. \tag{5.18}$$

This equation can then be solved in the following manner,

$$\frac{2a}{\xi^2}\,\mathrm{d}a - \frac{(\sigma_0^2+2\phi\nu t)}{2a}\,\mathrm{d}a = \phi\nu\,\mathrm{d}t. \tag{5.19}$$

$$\int\frac{2a^2}{\xi^2}\,\mathrm{d}a - \int\frac{\sigma_0^2}{2}\,\mathrm{d}a = \int(\phi\nu a\,\mathrm{d}t + \phi\nu t\,\mathrm{d}a) = \phi\nu\int\mathrm{d}(at) \tag{5.20}$$

$$\frac{2a^3}{3\xi^2} - \frac{\sigma_0^2 a}{2} - \phi\nu a t + C = 0, \tag{5.21}$$

where C is the constant of integration. Considering the initial value of the ring spacing as a_0, we get

$$C = -\left(\frac{2}{3\xi^2}\right)\left\{a_0^3 - \frac{3}{4}(\xi\sigma_0)^2 a_0\right\} = -a_0^3\left(\frac{2}{3\xi^2}\right)\left\{1-\frac{3}{4}\left(\frac{\xi\sigma_0}{a_0}\right)^2\right\}. \tag{5.22}$$

https://doi.org/10.1017/jfm.2017.815 Published online by Cambridge University Press

Thus, the above equation becomes

$$a^3 - \frac{3\xi^2}{2}\left(\frac{\sigma_0^2}{2} + \phi\nu t\right) a - a_0^3\left\{1 - \frac{3}{4}\left(\frac{\xi\sigma_0}{a_0}\right)^2\right\} = 0. \tag{5.23}$$

This equation is a generalized cubic equation, with ring radius a as a variable. Solution of such cubic equations is non-trivial. Using our non-dimensional notations used in § 2, we get

$$(a^*)^3 - \tfrac{3}{4}\gamma_0^2(1 + t^*)a^* - (1 - \tfrac{3}{4}\gamma_0^2) = 0, \tag{5.24}$$

where γ_0 is given by $\gamma_0 = (\xi\sigma_0/a_0)$ while a^* and t^* carry their usual meanings. Thus, it can be seen that ring expansion is governed not solely by the viscous diffusion time scale t^*, but also through its product with the square of the ratio $(\xi\sigma_0/a_0)$. This points us to a new form of time scale which governs radial expansion, given by

$$t_r^* = \left(\frac{\xi\sigma_0}{a_0}\right)^2 \left(\frac{2\phi\nu t}{\sigma_0^2}\right) \tag{5.25}$$

$$t_r^* = \left(\frac{2\phi\xi^2\nu t}{a_0^2}\right). \tag{5.26}$$

Thus, for different sized non-buoyant vortex rings with geometrical similarity ($\gamma_0 = \text{const.}$) propagating in the same fluid, a ring with smaller radius will experience higher relative expansion rates and *vice versa*. Considering this, the parameter $\gamma_0 = (\xi\sigma_0/a_0) = (R_0/a_0)$ emerges as providing a much more comprehensive physical understanding than a mere geometrical ratio. From (2.24) and (5.26), it can be interpreted as

$$\frac{1}{\gamma_0^2} = \frac{a_0^2}{R_0^2} = \frac{\text{viscous vorticity diffusion time scale}}{\text{ring expansion time scale}}. \tag{5.27}$$

Further, it can be inferred from (5.14) that the rate of variation of the ring diameter is proportional to the rate of viscous dissipation, i.e. the rate of increase of the core size.

The above two equations (5.14) and (5.24) provide greater insights into the evolution of vortex rings. We see that, for thin rings, at $\gamma_0 \ll 1$, the rate of radial expansion is significantly lower than the rate of viscous dissipation. This precisely means that a^* will remain close to unity such that the vortex spacing a will be invariant in time. If we use this constant-a criteria in (1.5), we arrive at an expression for the propagation velocity which scales with t^{-1}, which perfectly satisfies the short-time evolution equations.

As a thin-core vortex evolves in time, its core radius R will expand continuously. This will also lead to a corresponding increase in the radial expansion velocity V_r according to (5.14). As this process continues, the radial expansion of the ring will start to influence its translational velocity. At sufficiently large times, when the second term in (5.24) dominates over the third term, a^* becomes proportional to $t^{1/2}$. Thus, the vortex velocity profile migrates from t^{-1} at short times to $t^{-3/2}$ at longer durations.

The above analysis can be utilized to further understand the impulse variation of vortex rings. The impulse of a self-propagating vortex ring is given by

$$I = \alpha\Gamma a^2 = \alpha\Gamma_0\sigma_0\left(\frac{a^2}{\sigma^2}\right) \tag{5.28}$$

https://doi.org/10.1017/jfm.2017.815 Published online by Cambridge University Press

$$\frac{\mathrm{d}I}{\mathrm{d}t} = \alpha \Gamma_0 \sigma_0^2 \left[\frac{2a\sigma \left(\dfrac{\mathrm{d}a}{\mathrm{d}t} \right) - 2a^2 \left(\dfrac{\mathrm{d}\sigma}{\mathrm{d}t} \right)}{\sigma^3} \right] \tag{5.29}$$

$$\frac{\mathrm{d}I}{\mathrm{d}t} = \alpha \Gamma_0^2 \sigma_0^2 (2a^2) \left[\frac{\dfrac{\gamma}{\xi} \left(\dfrac{\mathrm{d}a}{\mathrm{d}t} \right) - \left(\dfrac{\mathrm{d}\sigma}{\mathrm{d}t} \right)}{\sigma^3} \right]. \tag{5.30}$$

For $0 < R/a \ll 1$, when $(\mathrm{d}a/\mathrm{d}t) \ll (\mathrm{d}\sigma/\mathrm{d}t)$, from the above equation, we hypothesize that the impulse of vortex rings should continuously decrease. For small times, when vortex spacing remains constant, the impulse should decrease continuously in the form

$$\frac{\mathrm{d}I}{\mathrm{d}t} = \left[\frac{\alpha \Gamma_0^2 \sigma_0^2 (2a^2) \left(\dfrac{\mathrm{d}\sigma}{\mathrm{d}t} \right)}{\sigma^3} \right]. \tag{5.31}$$

This loss of impulse was also reported by Maxworthy (1972). He ascribed this loss to vorticity rejection to the wake. From (5.30), we also propose that this rate of impulse loss should vanish as time progresses, due to the balance between viscous dissipation and ring expansion. This precisely explains the mathematical form of the equations put forward for thick vortex rings, which are fundamentally built on the assumption of impulse conservation.

This explains the dynamics of non-buoyant vortex rings in the early- and moderate-time regimes when the vortex undergoes constant mass entrainment. In reality, vortex rings constantly undergo short- and long-wavelength instabilities due to strain induced on the cores as a result of convection motion (Tsai & Widnall 1976; Jacquin *et al.* 2003). As the vorticity distribution spreads out, increasing its aspect ratio, or γ, short-wave instabilities increase exponentially, giving rise to secondary structures which lead to rapid vorticity decay, fluid detrainment and a transition to turbulence.

During this long-time regime, when vortex rings undergo net mass detrainment, the above theory predicts the shrinkage of vortex rings, as explained before. This phenomenon has also been observed and reported in many experimental and numerical studies (Hill 1975; Nomura *et al.* 2006). Flow visualization pictures (figure 7) obtained for one of our experimental cases clearly shows this behaviour.

Equations (5.14) and (5.24) explain in detail the complex mechanism governing ring expansion. However, considering their complexity, these equations are not considered while deriving equations (2.34) to (2.35). We believe that such an attempt would make the solutions mathematically complex and visually unappealing, which would undermine the aim of this study. None the less, for considerably thick vortices where $\gamma_0 \to 1$ and the impulse remains roughly constant, we see that the equations stated in § 2 provide a good approximation for the observed phenomenon.

This novel approach thus provides a unification of the early and late regimes of vortex lifetime, and many previously observed anomalous phenomena can be qualitatively and mathematically explained.

5.3. *Testing the fit of theory*

The equations derived in § 2 show a gradual deviation from the experimental values for larger times. To understand this aspect quantitatively, we have performed a test of

https://doi.org/10.1017/jfm.2017.815 Published online by Cambridge University Press

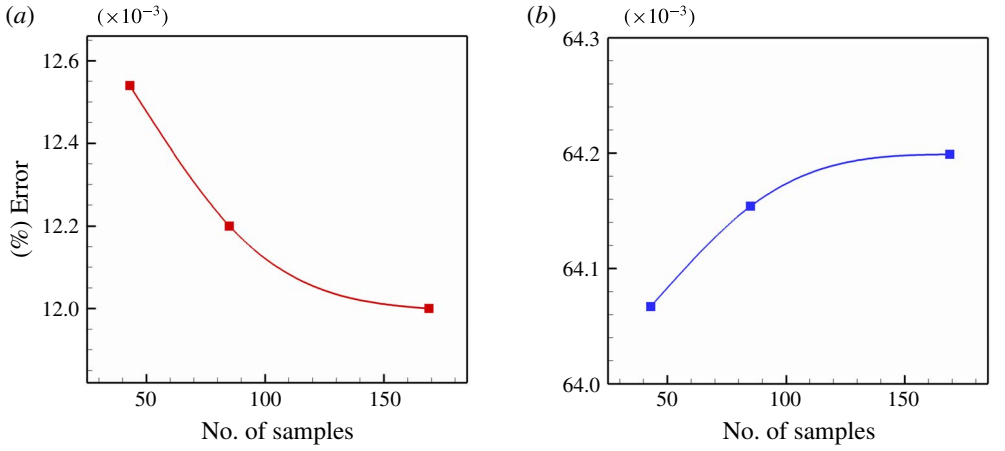


FIGURE 18. (Colour online) Mean dataset errors: (*a*) training set, (*b*) cross-validation set.

the fit for our primary variable ω_{max}. The entire dataset is divided into two parts, the training set and the cross-validation set, roughly in the ratio 60 : 40. Details about this approach are given in appendix B. Mean training set and cross-validation set errors for the experimental case C2-60 are plotted for an increasing number of dataset points (figure 18). Graphs for the other cases also show a similar trend.

Errors in the cross-validation set are relatively higher than in the training set. This difference increases with an increase in the number of dataset points. In data-analysis terms, this condition is known as high variance. Such behaviour signifies underfitting, and indicates the need for higher-order terms in order to explain the observed phenomenon.

5.4. *Comments on the value of* ϕ

The equations derived in § 2 have been acquired considering ϕ to remain constant throughout the evolution phase. However, from table 2, we see that the value of ϕ that best describes the motion varies with Reynolds number. Hence, in reality, as the vortex slows down during propagation and Re changes continuously, the value of ϕ also changes accordingly:

$$\phi = f(\omega_{max}, \sigma, \nu). \tag{5.32}$$

Realizing this time-varying nature of ϕ, one could account for the observed higher-order behaviour, and thus provide a better fit.

6. Conclusion

This study provides enhanced physical insights into the mechanism governing vortex evolution using a novel and effective mathematical framework. The ideas presented here are simple enough to form a part of an undergraduate textbook, but at the same time, it provides elegant and profound physical understanding of many observed, but so far unexplained phenomena. Approach used in this study carefully scrutinize and signify the role played by various vortex parameters, and many important inferences can be drawn.

Firstly, it shows that vorticity evolution is primarily governed by viscous diffusion, with negligible influence of vortex inertia. Also, for Reynolds numbers ranging

https://doi.org/10.1017/jfm.2017.815 Published online by Cambridge University Press

between 100 and 10000, the vortex core can be approximated to be circular without much loss of accuracy. Theoretical expressions derived in § 2 effectively explain the temporal variation in peak vorticity and core size as observed in experiments. This study also challenges the accepted theories of vorticity decay and suggests an alternate understanding into this subject. It provides a quantitative measure of circulation reduction which was hitherto unaddressed.

The transitional theory described in § 5.2 sheds light on the precise role of the Reynolds number and slenderness ratio in the vortex evolution mechanism. The vortex Reynolds number governs the rate of viscous dissipation of vorticity, which results in core expansion. This increase in core size is, however, independent of the slenderness ratio (R/a). On the other hand, the slenderness ratio plays a major role in ring expansion, with minimal influence of the Reynolds number. This addresses the long-standing confusion.

To be precise, the absolute extent of core expansion (σ) and ring expansion (a) are governed independently by the following two time scales

$$t^* = \frac{2\phi\nu t}{\sigma_0^2} \quad \text{and} \quad t_a^* = \frac{2\phi\nu t}{a_0^2}, \tag{6.1a,b}$$

whereas

$$A = \frac{t^*}{t_a^*} = \left(\frac{a_0}{\sigma_0}\right)^2, \tag{6.2}$$

which is a function of the slenderness ratio, signifies only the relative expansion rates. Moreover, this study concludes that vortex ring evolution can be classified into three phases. For $A > 100$, ring expansion is negligible and short-time behaviour can be observed. This can be termed as the 'nascent' stage, where the velocity follows (1.2). On the other hand, for $A < 10$, the vorticity diffusion rate is comparable to the ring expansion. This is the 'matured' stage, when velocity follows '$t^{-3/2}$' law. Between these two extremes, no single time scale governs the vortex ring evolution. Thus, this theory forms a bridge between the existing asymptotic theories, and the above time scales rationalize many anomalous observations reported in the literature.

In addition to the above, § 2 displays a new approach for studying self-similarity problems. Though we have addressed vorticity diffusion only, the same approach can be used for studying other phenomena as well.

Finally, some phenomena such as elliptical core, short- and long-wavelength instabilities have also been observed in the experiments. These are, however, not discussed due to their complex nature and miniscule advantage, over and above the present, for understanding the underlying physics. Nevertheless, our theory offers a comprehensive understanding of many of the observed phenomenon, and promises important applications.

This study can be utilized for understanding the evolution of aircraft wing tip vortices and could help in determining better air traffic standards. The methods used in § 2 can also be extended further to analyse equations with momentum and energy source and sink terms, which physically describe the mechanisms governing tornadoes and hurricanes, for example. An accurate understanding of the time-varying nature of vortex size and strength because of this attempt, could prove instrumental for gauging weather forecasts, leading to better disaster management with a direct impact on human life.

https://doi.org/10.1017/jfm.2017.815 Published online by Cambridge University Press

Acknowledgements

We gratefully acknowledge funding and support received from Solar Energy Research Institute for India and the United States (SERIIUS) and DST-SERI-Project no. DST/TMC/SERI/FR/136.

Supplementary material

Supplementary material is available at https://doi.org/10.1017/jfm.2017.815.

Appendix A. Gradient inversion method for finding the best-fit curve

This is an in-house technique used for finding the best-fit parameter (ϕ) in § 4 based on experimentally obtained values. We are familiar with the optimization of a continuous function where local stagnation points are obtained when the first derivative of the objective function (Z) vanishes i.e.

$$\frac{\mathrm{d}Z(x)}{\mathrm{d}x} = 0 \tag{A 1}$$

$$z = \sum_{i=1}^{n} |Y_{x_i} - f(x_i)|, \tag{A 2}$$

where n is the total sample size; $Y(x_i)$ is the experimentally obtained value of Y at $x = x_i$ and $f(x)$ is our analytical equation. However, the above-mentioned calculus approach of optimization is suitable only for continuous functions and is ineffective for discrete datasets where the derivative (A 1) may always carry a non-zero value. Other statistical techniques, such as stochastic and deterministic gradient descent, are also of limited use since their accuracy depends upon a predetermined minimum acceptable error value, which is difficult to comprehend for varying experimental conditions. Thus, a novel and robust method of local optimization is developed to satisfy our requirements, which is given below.

1. Start
2. Initialize parameter β, k, $\mathrm{d}\beta$
3. Start-loop: calculate sum Z
4. $\beta = \beta + k(\mathrm{d}\beta)$
5. If $Z_\beta > Z_{\beta+k(\mathrm{d}\beta)}$, $k = 1$ else $k = (-1)$
6. If k changes sign a second time: break
7. Else: Go to Start-loop
8. Return β
9. End

The above algorithm was coded in MATLAB. Under this method, local minimization of Z is reported when the gradient undergoes sign reversal for the second time. Using a constant and user-defined value of $\mathrm{d}\beta$, this program helps us to gain the desired resolution on the independent variable value (β here), thus overcoming the shortcomings of the other methods.

Appendix B. Test of fit

In order to validate our theoretical expressions, we have conducted a test-of-fit analysis using our experimental data and the best-fit equations. For this attempt, the

https://doi.org/10.1017/jfm.2017.815 Published online by Cambridge University Press

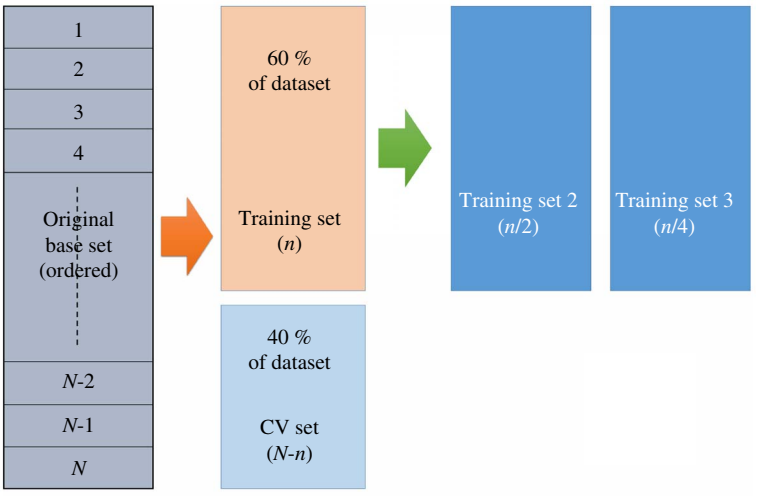


FIGURE 19. (Colour online) Schematic explaining the process of testing the hypothesis.

entire dataset of primary variable (vorticity here) is divided into two separate sets: 'training set' and 'cross-validation set', in the ratio 60 : 40, respectively (figure 19). The theoretical expression is fitted onto the base set using the technique described in appendix A.

The obtained best fit equation is then tested to check its validity on the cross-validation set. A measure of fit of an equation is quantified by the mean absolute error, given by

$$E = \frac{1}{n}\sum_{i=1}^{n} |Y_i - f(x_i)|. \tag{B 1}$$

The above error is calculated on both the base set and cross-validation set for different sample sizes of 100 %, 50 % and 25 %. Error values for different cropped sets are then compiled with an increasing number of sample points, as shown in figure 17.

For a good fit, the individual errors in 'base set' will continue to decrease and flatten as the number of sample points is increased. However, when these error values are significantly lower than that in the CV set, it indicates that the analytical equation satisfies the observed behaviour only for the short period and deviates at later stages. Moreover, when the CV set errors increase nonlinearly with an increase in the number of sample points, it bolsters the understanding that higher-order behaviour is prevalent which can only be captured by incorporating higher orders of the variables. This condition is known as 'variance'.

REFERENCES

ADVAITH, S., MANU, K. V., TINAIKAR, A., CHETIA, U. K. & BASU, S. 2017 Interaction of vortex ring with a stratified finite thickness interface. *Phys. Fluids* **29** (9), 093602.

ARCHER, P. J., THOMAS, T. G. & COLEMAN, G. N. 2008 Direct numerical simulation of vortex ring evolution from the laminar to the early turbulent regime. *J. Fluid Mech.* **598**, 201–226.

https://doi.org/10.1017/jfm.2017.815 Published online by Cambridge University Press

ARVIDSSON, P. M., KOVÁCS, S. J., TÖGER, J., BORGQUIST, R., HEIBERG, E., CARLSSON, M. & ARHEDEN, H. 2016 Vortex ring behavior provides the epigenetic blueprint for the human heart. *Sci. Rep.* **6**, 22021.

AUERBACH, D. 1988 Some open questions on the flow of circular vortex rings. *Fluid Dyn. Res.* **3** (1–4), 209–213.

BARENBLATT, G. I. 1996 *Scaling, Self-similarity, and Intermediate Asymptotics: Dimensional Analysis and Intermediate Asymptotics,* vol. 14. Cambridge University Press.

BATCHELOR, G. K. 2000 *An Introduction to Fluid Dynamics*. Cambridge University Press.

BERGDORF, M., KOUMOUTSAKOS, P. & LEONARD, A. 2007 Direct numerical simulations of vortex rings at $Re_{gamma} = 7500$. *J. Fluid Mech.* **581**, 495–505.

BOND, D. & JOHARI, H. 2010 Impact of buoyancy on vortex ring development in the near field. *Exp. Fluids* **48** (5), 737–745.

CANTWELL, B. & ROTT, N. 1988 The decay of a viscous vortex pair. *Phys. Fluids* **31** (11), 3213–3224.

CATER, J., SORIA, J. & LIM, T. T. 1998 The vorticity of a vortex ring core. In *Proceedings of the 13th Australasian Fluid Mechanics Conference, Melbourne, Australia*, pp. 5–8. Monash University Publishing.

DABIRI, J. O. 2009 Optimal vortex formation as a unifying principle in biological propulsion. *Annu. Rev. Fluid Mech.* **41**, 17–33.

DABIRI, J. O. & GHARIB, M. 2005 The role of optimal vortex formation in biological fluid transport. *Proc. R. Soc. Lond.* B **272** (1572), 1557–1560.

DAHM, W. J. A., SCHEIL, C. M. & TRYGGVASON, G. 1989 Dynamics of vortex interaction with a density interface. *J. Fluid Mech.* **205**, 1–43.

DENGLER, K. & REEDER, M. J. 1997 The effects of convection and baroclinicity on the motion of tropical-cyclone-like vortices. *Q. J. R. Meteorol. Soc.* **123** (539), 699–725.

DIDDEN, N. 1979 On the formation of vortex rings: rolling-up and production of circulation. *Z. Angew. Math. Phys.* **30** (1), 101–116.

DYSON, F. W. 1893 The potential of an anchor ring. Part II. *Phil. Trans. R. Soc. Lond.* A **184**, 1041–1106.

DZIEDZIC, M. & LEUTHEUSSER, H. J. 1996 An experimental study of viscous vortex rings. *Exp. Fluids* **21** (5), 315–324.

EMANUEL, K. 2005 Increasing destructiveness of tropical cyclones over the past 30 years. *Nature* **436** (7051), 686–688.

FOHL, T. 1967 Optimization of flow for forcing stack wastes to high altitudes. *J. Air Pollut. Control Assoc.* **17** (11), 730–733.

FRAENKEL, L. E. 1972 Examples of steady vortex rings of small cross-section in an ideal fluid. *J. Fluid Mech.* **51** (01), 119–135.

FUKUMOTO, Y. & KAPLANSKI, F. 2008 Global time evolution of an axisymmetric vortex ring at low Reynolds numbers. *Phys. Fluids* **20** (5), 053103.

FUKUMOTO, Y. & MOFFATT, H. K. 2000 Motion and expansion of a viscous vortex ring. Part 1. A higher-order asymptotic formula for the velocity. *J. Fluid Mech.* **417**, 1–45.

GHARIB, M., RAMBOD, E., KHERADVAR, A., SAHN, D. J. & DABIRI, J. O. 2006 Optimal vortex formation as an index of cardiac health. *Proc. Natl Acad. Sci. USA* **103** (16), 6305–6308.

GHARIB, M., RAMBOD, E. & SHARIFF, K. 1998 A universal time scale for vortex ring formation. *J. Fluid Mech.* **360**, 121–140.

HELMHOLTZ, H. 1858 About integrals of hydrodynamic equations related with vortical motions. *J. Reine Angew. Math.* **55**, 25.

HILL, F. M. 1975 A numerical study of the descent of a vortex pair in a stably stratified atmosphere. *J. Fluid Mech.* **71**, 1–13.

HILL, M. J. M. 1894 On a spherical vortex. *Proc. R. Soc. Lond.* A **55** (331–335), 219–224.

JACQUIN, L., FABRE, D., SIPP, D., THEOFILIS, V. & VOLLMERS, H. 2003 Instability and unsteadiness of aircraft wake vortices. *Aerosp. Sci. Technol.* **7** (8), 577–593.

https://doi.org/10.1017/jfm.2017.815 Published online by Cambridge University Press

JOHARI, H. & FANG, H. 1997 Horizontal vortex ring motion in linearly stratified media. *Phys. Fluids* **9** (9), 2605–2616.

KEANE, R. D. & ADRIAN, R. J. 1990 Optimization of particle image velocimeters. I. Double pulsed systems. *Meas. Sci. Technol.* **1** (11), 1202.

KELVIN, L. 1867 On vortex atoms. *Proc. R. Soc. Edin.* **6**, 94–105.

LAMB, H. 1932 *Hydrodynamics*. Cambridge University Press.

LEE, J. S., PARK, S. J., LEE, J. H., WEON, B. M., FEZZAA, K. & JE, J. H. 2015 Origin and dynamics of vortex rings in drop splashing. *Nature Commun.* **6**.

LINDEN, P. F. 1973 The interaction of a vortex ring with a sharp density interface: a model for turbulent entrainment. *J. Fluid Mech.* **60**, 467–480.

LUGT, H. J. 1983 *Vortex Flow in Nature and Technology,* vol. 1. p. 305. Wiley-Interscience.

MANU, K. V., ANAND, P., CHETIA, U. K. & BASU, S. 2015 Effects of instabilities and coherent structures on the performance of a thermocline based thermal energy storage. *Appl. Therm. Engng* **87**, 768–778.

MAXWORTHY, T. 1972 The structure and stability of vortex rings. *J. Fluid Mech.* **51** (01), 15–32.

MAXWORTHY, T. 1977 Some experimental studies of vortex rings. *J. Fluid Mech.* **81** (03), 465–495.

MOORE, D. W. & SAFFMAN, P. G. 1973 Axial flow in laminar trailing vortices. *Proc. R. Soc. Lond.* A **333**, 491–508.

NOMURA, K. K., TSUTSUI, H., MAHONEY, D. & ROTTMAN, J. W. 2006 Short-wavelength instability and decay of a vortex pair in a stratified fluid. *J. Fluid Mech.* **553**, 283–322.

ORLANDI, P., EGERMANN, P. & HOPFINGER, E. J. 1998 Vortex rings descending in a stratified fluid. *Phys. Fluids* **10** (11), 2819–2827.

OSEEN, C. W. 1910 Stokes' formula and a related theorem in hydrodynamics. *Ark. Mat. Astron. Fys.* **6**, 20.

OSHIMA, Y. 1972 Motion of vortex rings in water. *J. Phys. Soc. Japan* **32** (4), 1125–1131.

PULLIN, D. I. 1979 Vortex ring formation at tube and orifice openings. *Phys. Fluids* **22** (3), 401–403.

PULLIN, D. I. & SAFFMAN, P. G. 1998 Vortex dynamics in turbulence. *Annu. Rev. Fluid Mech.* **30** (1), 31–51.

RAFFEL, M., WILLERT, C. E., WERELEY, S. & KOMPENHANS, J. 2013 *Particle Image Velocimetry: A Practical Guide*. Springer.

RAYFIELD, G. W. & REIF, F. 1964 Quantized vortex rings in superfluid helium. *Phys. Rev.* **136**, A1194–A1208.

REYNOLDS, O. 1876 On the resistance encountered by vortex rings and the relation between vortex rings and the stream-lines of a disc. *Nature* **14**, 477–479.

SAFFMAN, P. G. 1970 The velocity of viscous vortex rings. *Stud. Appl. Maths* **49** (4), 371–380.

SAFFMAN, P. G. 1978 The number of waves on unstable vortex rings. *J. Fluid Mech.* **84** (04), 625–639.

SHE, Z.-S., JACKSON, E. & ORSZAG, S. A. 1990 Intermittant vortex structures in homogeneous isotropic turbulence. *Nature* **344** (6263), 226.

SMITH, R. K., MONTGOMERY, M. T. & ZHU, H. 2005 Buoyancy in tropical cyclones and other rapidly rotating atmospheric vortices. *Dyn. Atmos. Oceans* **40** (3), 189–208.

SOMMERFELD, A. 1950 *Lectures on Theoretical Physics, Vol. II: Mechanics of Deformable Bodies*. Academic.

SONIN, E. B. 2016 *Dynamics of Quantised Vortices in Superfluids*. Cambridge University Press.

SPALART, P. R. 1998 Airplane trailing vortices. *Annu. Rev. Fluid Mech.* **30**, 107–138.

SPEDDING, G. R., HEDENSTRÖM, A. & ROSÉN, M. 2003 Quantitative studies of the wakes of freely flying birds in a low-turbulence wind tunnel. *Exp. Fluids* **34** (2), 291–303.

STANAWAY, S. K., CANTWELL, B. J. & SPALART, P. R. 1988 A numerical study of viscous vortex rings using a spectral method.

SULLIVAN, I. S., NIEMELA, J. J., HERSHBERGER, R. E., BOLSTER, D. & DONNELLY, R. J. 2008 Dynamics of thin vortex rings. *J. Fluid Mech.* **609**, 319–347.

THOMSON, J. J. & NEWALL, H. F. 1885 On the formation of vortex rings by drops falling into liquids, and some allied phenomena. *Proc. R. Soc. Lond.* A **39**, 417–436.

https://doi.org/10.1017/jfm.2017.815 Published online by Cambridge University Press

TSAI, C.-Y. & WIDNALL, S. E. 1976 The stability of short waves on a straight vortex filament in a weak externally imposed strain field. *J. Fluid Mech.* **73** (04), 721–733.

TURNER, J. S. 1960 A comparison between buoyant vortex rings and vortex pairs. *J. Fluid Mech.* **7** (03), 419–432.

WAKELIN, S. L. & RILEY, N. 1997 On the formation and propagation of vortex rings and pairs of vortex rings. *J. Fluid Mech.* **332**, 121–139.

WATANABE, S., NAKAMICHI, K., JANG, I.-S., KAZAMA, K., HASEGAWA, S.-I. & ISHIWATA, S. 1995 Generation of a vortex ring with high Reynolds number by an exploding wire in water. *J. Phys. Soc. Japan* **64** (10), 3748–3757.

WEIGAND, A. & GHARIB, M. 1997 On the evolution of laminar vortex rings. *Exp. Fluids* **22** (6), 447–457.

WEIHS, D. 1973 Hydromechanics of fish schooling. *Nature* **241** (5387), 290–291.

WITELSKI, T. P. & BERNOFF, A. J. 1998 Self-similar asymptotics for linear and nonlinear diffusion equations. *Stud. Appl. Maths* **100** (2), 153–193.

https://doi.org/10.1017/jfm.2017.815 Published online by Cambridge University Press